Monthly Notices
of the
ROYAL ASTRONOMICAL SOCIETY

MNRAS **525,** 4388–4404 (2023) https://doi.org/10.1093/mnras/stad2564
Advance Access publication 2023 August 25

The MUSE Ultra Deep Field (MUDF). IV. A pair of X-ray weak quasars at the heart of two extended Lyα nebulae

Elisabeta Lusso, [1,2★] Emanuele Nardini, [2★] Michele Fumagalli, [3,4★] Matteo Fossati, [3,5] Fabrizio Arrigoni Battaia, [6] Mitchell Revalski, [7] Marc Rafelski, [7,8] Valentina D'Odorico, [9,10,11] Celine Peroux, [12,13] Stefano Cristiani, [4,11,14] Pratika Dayal, [15] Francesco Haardt [16] and Emma K. Lofthouse [3,5]

[1] Dipartimento di Fisica e Astronomia, Università di Firenze, via G. Sansone 1, I-50019 Sesto Fiorentino, Firenze, Italy
[2] INAF – Osservatorio Astrofisico di Arcetri, Largo Enrico Fermi 5, I-50125 Firenze, Italy
[3] Dipartimento di Fisica G. Occhialini, Università degli Studi di Milano-Bicocca, Piazza della Scienza 3, I-20126 Milano, Italy
[4] INAF - Osservatorio Astronomico di Trieste, via G. B. Tiepolo 11, I-34143 Trieste, Italy
[5] INAF - Osservatorio Astronomico di Brera, via Bianchi 46, I-23087 Merate (LC), Italy
[6] Max-Planck-Institut fur Astrophysik, Karl-Schwarzschild-Str 1, D-85748 Garching bei München, Germany
[7] Space Telescope Science Institute, 3700 San Martin Drive, Baltimore, MD 21218, USA
[8] Department of Physics and Astronomy, Johns Hopkins University, Baltimore, MD 21218, USA
[9] INAF–Osservatorio Astronomico di Trieste, Via G.B. Tiepolo, 11, I-34143 Trieste, Italy
[10] Scuola Normale Superiore, P.zza dei Cavalieri, I-56126 Pisa, Italy
[11] IFPU–Institute for Fundamental Physics of the Universe, via Beirut 2, I-34151 Trieste, Italy
[12] European Southern Observatory, Karl-Schwarzschildstrasse 2, D-85748 Garching bei München, Germany
[13] Aix Marseille Université, CNRS, LAM (Laboratoire d'Astrophysique de Marseille) UMR 7326, F-13388 Marseille, France
[14] INFN–National Institute for Nuclear Physics, via Valerio 2, I-34127 Trieste, Italy
[15] Kapteyn Astronomical Institute, Rijksuniversiteit Groningen, Landleven 12, Groningen, 9717 AD, the Netherlands
[16] DiSAT, Università degli Studi dell'Insubria,via Valleggio 11, I-22100 Como, Italy

Accepted 2023 August 22. Received 2023 August 22; in original form 2023 May 10

ABSTRACT

We present the results obtained from follow-up observations of the MUSE Ultra Deep Field (MUDF) at X-ray energies with *XMM–Newton*. The MUDF is centred on a unique field with two bright, physically associated quasars at $z \simeq 3.23$, separated by $\sim$500 kpc in projection. Both quasars are embedded within extended Lyα nebulae ($\gtrsim$100 kpc at a surface brightness flux level of $\approx 6 \times 10^{-19}$ erg s^{-1} cm^{-2} arcsec^{-2}), whose elongated morphology is suggestive of an extended filament connecting the quasar haloes. The new X-ray observations presented here allow us to characterize the physical properties (e.g. X-ray slope, luminosities, gas column densities) in the innermost region of the MUDF quasars. We find that both quasars are X-ray underluminous compared to objects at similar ultraviolet luminosities. Based on our X-ray spectral analysis, absorbing columns of $N_{\rm H}(z) \gtrsim 10^{23}$ cm^{-2} appear unlikely therefore such a weakness is possibly intrinsic. When also including literature data, we do not observe any detectable trend between the area of the nebulae and nuclear luminosities at both the rest-frame 2 keV and 2500 Å. The area is also not correlated with the X-ray photon index nor with the integrated band flux in the hard band (2–10 keV). We also do not find any trend between the extended Lyα emission of the nebulae and the nuclear X-ray luminosity. Finally, the properties of the MUDF quasars' nebulae are consistent with the observed relation between the Lyα integrated luminosity of the nebulae and their area. Our results suggest that the quasar ionization power is not a strong driver of the morphology and size of the nebulae.

Key words: galaxies: formation – galaxies: haloes – galaxies: high-redshift – quasars: general – X-rays: galaxies – X-rays: general.

1 INTRODUCTION

The current cosmological concordance model (ΛCDM) predicts that galaxies form in overdensities at the intersection of filaments, which compose the cosmic web (e.g. Bond, Kofman & Pogosyan 1996; Dayal & Ferrara 2018). This prediction is supported indirectly by observations of the large-scale structures traced with galaxy surveys (e.g. Reid et al. 2012; Anderson et al. 2014; Wisotzki et al. 2018; Malavasi et al. 2020) and by studies of the Lyα forest in absorption (e.g. McDonald et al. 2005). A valuable technique to map the gas distribution in the circumgalactic medium (CGM) has been through the direct imaging of the fluorescent Lyα line in emission around bright quasars (e.g. Cantalupo et al. 2014; Hennawi et al. 2015; Borisova et al. 2016; Arrigoni Battaia et al. 2018; Cai et al. 2019;

★ E-mail: elisabeta.lusso@unifi.it (EL); emanuele.nardini@inaf.it (EN); michele.fumagalli@unimib.it (MF)

Published by Oxford University Press on behalf of Royal Astronomical Society

Farina et al. 2019; Arrigoni Battaia et al. 2019a, b; O'Sullivan et al. 2020; Fossati et al. 2021) and galaxies (Leclercq et al. 2017; Wisotzki et al. 2018), where the integral field spectrographs positioned at the largest observing facilities, such as the Multi-Unit Spectroscopic Explorer (MUSE; Bacon et al. 2010) at the Very Large Telescope and the Keck Cosmic Web Imager (KCWI; Morrissey et al. 2018) at the Keck telescope, have been key to significantly improve the detection of this extended Lyα emission (see also e.g. Umehata et al. 2019; Bacon et al. 2021; Kusakabe et al. 2022; Lujan Niemeyer et al. 2022).

Understanding the ionizing source of extended Lyα nebulae requires multi-wavelength data as obscured AGN, for instance, can be missed at UV energies (e.g. Geach et al. 2009). Indeed, rest-frame UV-based surveys are blind to dust obscured quasars, whilst X-rays (together with radio wavelengths) can help to constrain the presence (or not) of possible sources associated to extended Lyα emission (see Cantalupo 2017, for a review on the topic).

Lyα nebulae have not yet been systematically targeted with deep X-ray observations, as the presence of a hard ionizing source, the quasar, is usually taken for granted. However, X-ray explorations have been conducted to understand the nature of the so-called Lyα blobs (LABs; Steidel, Pettini & Adelberger 2001), in which the identification of the powering sources turned out to be difficult. To our knowledge, the only field with deep X-ray coverage in the literature is the small selected area 22h (SSA22) field (Lilly, Cowie & Gardner 1991; Steidel et al. 1998). SSA22 is an overdense region at $z = 3.1$ known to host several LABs (e.g. Matsuda et al. 2004). The field has been extensively studied at several wavelengths. The first evidence of embedded powering sources in the LABs came from the detection of bright submillimetre objects with a bolometric luminosity in excess of 10^{12} $L_{\odot}$ (e.g. Chapman et al. 2001; Geach et al. 2005). No evidence from deep *Chandra* X-ray observations of a clear X-ray counterpart was found (Chapman et al. 2004), yet the possibility of a luminous but heavily obscured AGN along our line of sight was not excluded. By analysing the same data, Basu-Zych & Scharf (2004) discovered a hard-band X-ray source in a second giant Lyα emission nebula in the SSA22 region. They confirmed that the nebula with significant submillimetre output is undetected at the X-ray energies, while the other is a factor of 2–10 times less bright in the submillimetric but appears to contain a highly obscured AGN. Neither of these two Lyα nebulae was associated with conspicuous radio emission. With even deeper *Chandra* observations (400 ks), Lehmer et al. (2009) found a total of five X-ray detected sources in 158 Lyα emitters in the SSA22 field, implying a larger fraction of AGN activity than in lower density environments (see also Monson et al. 2023).

Nilsson et al. (2006) published the discovery of a Lyα nebula at $z \simeq 3.157$ in the Great Observatories Origins Deep Survey (GOODS) South field, which is rich in multiwavelength data from the X-rays with *Chandra* to the infrared with *Spitzer*. Intriguingly, unlike other known Lyα extended nebulae, the deep GOODS imaging of the nebulae displayed no associated continuum counterparts in any band, from the X-rays to the infrared, suggesting that the most probable origin of the extended Lyα emission could be cold accretion onto a dark matter halo rather than an AGN. This scenario, however, was later disproved by the detection of six continuum sources associated with the nebula and a nearby obscured AGN (Prescott et al. 2015), which actually turns out to be located at the centre of a larger Lyα structure (Sanderson et al. 2021).

LABs are also found at much lower redshifts. Kawamuro et al. (2017) presented *NuSTAR* hard X-ray (3–30 keV) observations, complemented with *Chandra* and *Swift* data, of the two X-ray brightest sources at $z \simeq 0.3$ that show extended Lyα emission, SDSS J011341.11+010608.5 and SDSS J115544.59−14739.9 (Schirmer et al. 2016). *NuSTAR* data revealed the presence of bright X-ray emission in both sources, with 2–10 keV luminosity (0.5–3) $\times$ 10^{44} erg s^{-1} and moderate obscuration ($N_{\rm H} \sim 0.6$–5×10^{23} cm^{-2}).

In this framework, our group designed an observational campaign to acquire very deep observations with MUSE in a $\approx$1.2 $\times$ 1.4 arcmin^2 region centred at RA=21:42:24 and Dec = −44:19:48 (hereafter the MUSE Ultra Deep Field or MUDF). The MUDF hosts several astrophysical structures at different redshifts, including two physically associated quasars at $z \approx 3.23$, J214225.78−442018.3, and J214222.17−441929.8 (hereafter J2142−4420 and J2142−4419, respectively), with a projected separation of $\approx$1 arcmin (or $\approx$500 kpc at $z \approx 3$). Another quasar with similar redshift lies at $\approx$8 arcmin separation (LBQS 2138−4427), making this system a quasar triplet (Francis & Hewett 1993). In the first paper of this series, Lusso et al. (2019a) studied the morphology of the extended Lyα nebulae surrounding the quasars, observing that the ionized gas is elongated along the line connecting the two sources. In the second paper, Fossati et al. (2019) studied the galaxy environment and gaseous properties of the seven galaxy groups detected at redshifts $0.5 < z < 1.5$ with halo mass in the interval $\log{(M_{\rm h}/{\rm M}_{\odot})} \simeq 11$–$13.5$. The absorption strength associated with these groups is higher than that of near-isolated galaxies at similar mass and impact parameters. Additionally, no evidence was found for widespread cool gas that could be associated with a diffuse intra-group medium. In the third paper, Revalski et al. (2023) utilized the extensive wavelength coverage of MUSE and WFC3 to measure spectroscopic redshifts for 419 sources down to galaxy stellar masses of $\log{({\rm M}/{\rm M}_{\odot})} \simeq 7$ at $z \simeq 1$–2, and publicly released the calibrated *Hubble Space Telescope* (*HST*) observations, catalogues, and associated data products.[1]

In this paper, we present the *XMM–Newton* observation of the MUDF, which provides the first view at high energies of the assembly of a potentially massive $z \simeq 3.2$ overdensity in this field. Our main goal is to characterize the physical properties (e.g. X-ray slope, luminosities, gas column densities) in the innermost region of quasars with physically associated and extended Lyα nebulae.

The paper is structured as follows: in Section 2, we present the MUDF and *XMM–Newton* observations and data reduction, whilst the X-ray and the UV spectral analyses are discussed in Sections 3 and 4, respectively. Section 5 is devoted to the presentation of the results and their discussion, with conclusions drawn in Section 6. Whenever luminosity values are reported, we have assumed a standard flat ΛCDM cosmology with $\Omega_{\rm M} = 0.3$ and $H_0 = 70$ km s^{-1} Mpc^{-1}.

2 OBSERVATIONS AND DATA REDUCTION

2.1 The MUSE Ultra Deep Field data

The MUDF is covered by $\approx$140 h of MUSE data (ESO PID 1100.A−0528, see Fossati et al. 2019, for details about the survey design, the MUSE observations and data reduction; Fossati et al. in preparation for the presentation of the final data set), with $\approx$100 h in the centremost region. This program is complemented by deep high-resolution spectroscopy of the quasars with UVES (Ultraviolet Visual Echelle Spectrograph; Dekker et al. 2000) at the VLT (ESO PIDs 65.O−0299, 68.A−0216, 69.A−0204, 102.A−0194; D'Odorico, Petitjean & Cristiani 2002), and by a very deep spectroscopic survey (90 orbits in a single field) in the near-infrared with the Wide Field

---

[1] https://archive.stsci.edu/hlsp/mudf

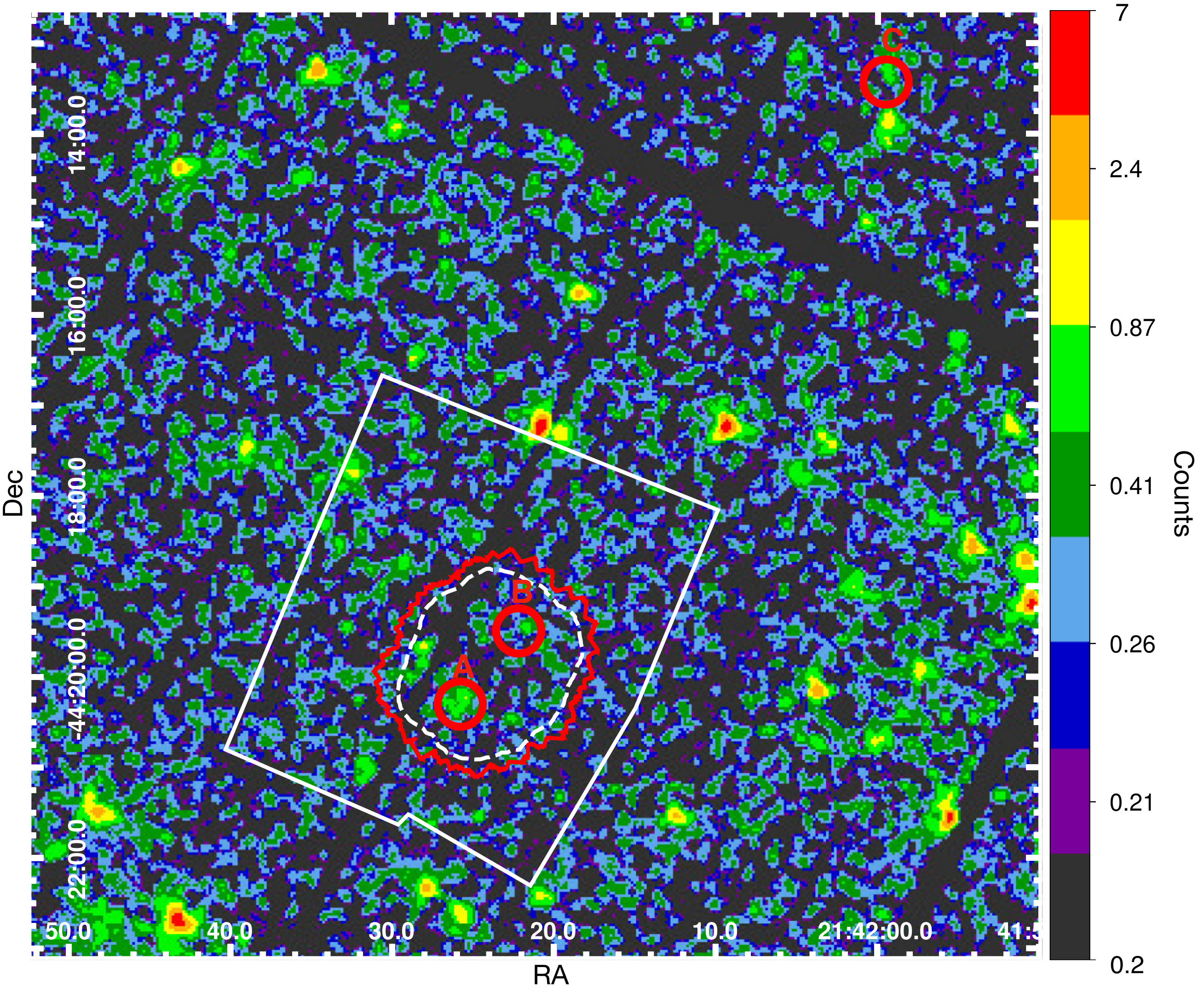

Figure 1. *XMM–Newton* MOS2 (Metal Oxide Semiconductor) image at 0.5–5 keV. The area marked with the white solid line represents the *F140W*/*HST* coverage (Revalski et al. 2023). The solid red line represents the MUDF covered with MUSE, whilst the white dashed lines marks the region with at least 4 h of exposure with MUSE. The red circles mark the locations of the primary quasars and have radii of ∼15 arcsec. The image is spatially rebinned and smoothed through a Gaussian function. Labels A, B, and C as in Table 1. The (cleaned) *XMM–Newton* images for the pn, MOS1, and MOS2 CCDs that cover the 0.2–12 keV energy band (i.e. EPIC band 8) of the MUDF can be accessed through MAST at https://archive.stsci.edu/hlsp/mudf.

Camera 3 (WFC3) instrument on board the *HST* (Revalski et al. 2023), together with deep eight-orbit near UV imaging (program IDs: 15637, PI: M. Rafelski; and 15968, PI: M. Fossati). Specifically, the MUDF has been observed with the WFC3/IR with the G141 grism and the *F140W* filter, which covers a spectral range of 10750–17000 Å, and thus extends the MUSE spectroscopic data in the rest-frame UV, with a resolving power of $R \simeq 150$ at 14 000 Å. We refer to Revalski et al. (2023) for details on the program design and acquisition of the *HST* observations.

2.2 The X-ray data

XMM–Newton targeted the MUDF for a full orbit (revolution 3731, duration 139 ks; PI: E. Lusso) on 2020 April 22, with the three EPIC (European Photon Imaging Camera) cameras (Strüder et al. 2001; Turner et al. 2001) operating in Full Frame mode with thin optical filter. The event files were reprocessed with the Science Analysis System (SAS) v19.1.0, following the standard procedures and using the latest calibration files. The final part of the observation was affected by background flares, hence the good time intervals have been created by imposing a count rate threshold for high-energy single-pixel events of 0.4 $\mathrm{s^{-1}}$ (10–12 keV) and 0.35 $\mathrm{s^{-1}}$ (>10 keV) over the whole pn and MOS detectors,[2] respectively. After the dead-time correction and background filtering, the net exposures are 94.8 ks for pn, 128.5 ks for MOS1, and 128.6 ks for MOS2.

The source spectra were extracted from circular regions centred at the nominal optical coordinates of each target of interest, with radii of 15 arcsec for J2142−4420 (and LBQS 2138−4427) and 12 arcsec for J2142−4419, corresponding to an encircled energy fraction of ≲70 per cent. Although a non-negligible fraction of counts might be lost,[3] such apertures are required due to the presence of

---

[2] https://www.cosmos.esa.int/web/xmm-newton/technical-details-epic

[3] Note that this ‘aperture loss’ is corrected for at the spectral analysis stage by the ancillary response files, which store all the *geometrical* information relative to the source extraction position on each detector (e.g. effective area, quantum efficiency, vignetting).

Table 1. Summary of the properties of the MUDF quasars.

Object	$z_{\rm sys}$	$(\nu L_\nu)_{\rm UV}$ ^{a} erg s^{-1}	$(\nu L_\nu)_{\rm X}$ ^{b} erg s^{-1}	$(\nu L_\nu)_{\rm CIV}$ ^{c} erg s^{-1}	Cts^d	$\Gamma_{\rm X}^e$	$(\nu F_\nu)_{2\,\rm keV}$ ^{f} erg s^{-1} cm^{-2}	C/ν^g	$(\nu F_\nu)_{2\,\rm keV,exp}$ ^{h} erg s^{-1} cm^{-2}
(A) J2142−4420	3.229 ± 0.003	78.5	$6.10^{+1.33}_{-1.18}$	1.07	224 ± 23	1.06 ± 0.14	$0.66^{+0.14}_{-0.13}$	403/433	15.5
(B) J2142−4419	3.221 ± 0.004	6.5	$3.54^{+1.81}_{-1.42}$	0.18	67 ± 18	$1.73^{+0.53}_{-0.44}$	$0.38^{+0.20}_{-0.15}$	240/263	2.9
(C) LBQS 2138−4427	$\approx$3.170	–	$6.64^{+1.64}_{-1.42}$	–	136 ± 20	1.11 ± 0.17	$0.75^{+0.19}_{-0.15}$	316/301	–

Note.^{a} Continuum luminosity at rest-frame 2500 Å normalized to 10^{45} erg s^{-1}. Statistical uncertainties are less than 1 per cent. ^{b} Continuum luminosity at rest-frame 2 keV normalized to 10^{43} erg s^{-1}. ^{c} Integrated C IV luminosity normalized to 10^{45} erg s^{-1}. Statistical uncertainties are smaller than 1 per cent. ^{d} *XMM–Newton*/EPIC net counts in the 0.3–7 keV band. ^{e} Best-fit photon index of the continuum in the baseline model (see Section 3 for details). ^{f} Observed flux at rest-frame 2 keV, corrected for Galactic absorption and normalized to 10^{-15} erg s^{-1} cm^{-2}. ^{g} Best-fit statistics of the baseline model: C and ν represent the C-statistics and degrees of freedom, respectively. ^{h} Expected flux (in units of 10^{-15} erg s^{-1} cm^{-2}) at rest-frame 2 keV obtained by assuming the $L_{\rm X}$–$L_{\rm UV}$ relation published by Lusso et al. (2020).

nearby point-like or diffuse emission structures that would otherwise contaminate the source spectra (see Fig. 1 and Section 3.1). The background was evaluated on nearby regions free of excess emission, with radii of 40–60 arcsec depending on the target and detector. The total number of collected net counts is provided for each source in Table 1. We note that LBQS 2138−4427 falls outside the MOS1 field of view, while in the pn image J2142−4420 partly falls on the gap between two adjacent chips, thus reducing the actual effective area. The appropriate response files were generated with the SAS tasks RMFGEN and ARFGEN.

The spectral analysis was performed over the 0.3–7 keV band with the XSPEC v12.12.0 fitting package (Arnaud 1996). The spectra are fully background-dominated at higher energies, and changing the upper end of the fitting range has no effect on the results. Given the limited statistics, the spectra were binned to ensure a minimum of one count per energy channel, and a modified version of the Cash statistic was adopted (*cstat* or W-statistic in XSPEC; Cash 1979; Kaastra 2017), as appropriate for source and background data in the Poissonian regime. The uncertainties we provide on the model parameters, including fluxes, correspond to $\Delta C = 1$, unless stated otherwise. The fits were simultaneously carried out on the individual spectra from the three EPIC detectors. Yet, for visual purposes, we also generated a merged EPIC spectrum with the SAS task EPICSPECCOMBINE (see Fig. 2).

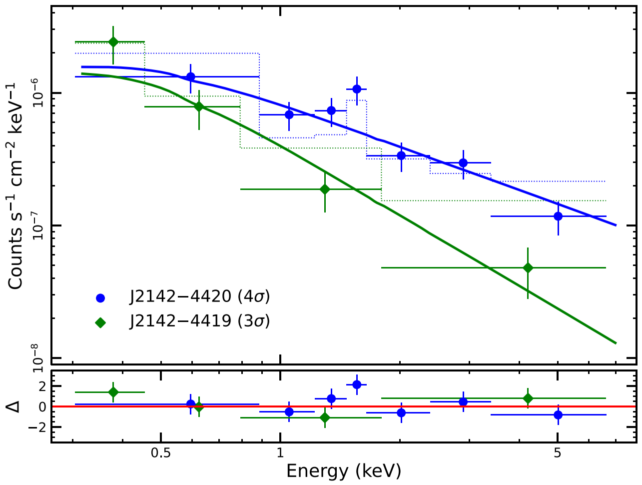

Figure 2. Combined *XMM–Newton* EPIC spectra of J2142−4420 (blue dots) and J2142−4419 (green diamonds), binned for visual clarity to a 4σ and 3σ significance, respectively. The best power-law fits are represented by the solid curves, while the dotted lines indicate the background levels. Residuals are computed as $\Delta = $ (data−model)/error and are shown in the bottom panel. Note that the line-like excess around 1.6 keV in the spectrum of J2142−4420, although corresponding to the Fe K band in the rest frame, is most likely an instrumental artefact, as discussed in the text. The red line refers to $\Delta = 0$.

3 X-RAY SPECTRAL ANALYSIS

Before embarking on the analysis of the X-ray spectra of the quasar pair, we note that both sources are significantly fainter (by roughly an order of magnitude) than expected. In fact, as no deep X-ray observation of this field was available before the current *XMM–Newton* programme, we had estimated preliminary count rates by converting the rest-frame monochromatic luminosities at 2500 Å (Table 1), from the WFC3 spectra, into those at 2 keV through the correlation of Lusso & Risaliti (2016). Based on this, we should have collected at least several hundred net counts also from the fainter object, thus allowing a robust determination of the X-ray spectral parameters. This is clearly not the case, even considering the unfortunate position of J2142−4420 near a gap on the pn detector (see Fig. 1 and Section 2). As a consequence, the components of the quasar pair must be either highly absorbed or intrinsically weak in the X-rays.

Given the limited data quality, we first modelled the spectra with a simple power law modified by Galactic absorption, fixed at 1.63×10^{20} cm^{-2} (HI4PI Collaboration et al. 2016). The fit is statistically acceptable for both quasars (Table 1), and the photon index of $\Gamma_{\rm X} \sim 1.7$ for J2142−4419 is fully consistent with the typical values found in AGN with negligible X-ray absorption (e.g. Young, Elvis & Risaliti 2009; Scott et al. 2011), although the nominal 1σ confidence range is rather large ($\sim$ 1.3–2.3). The spectral slope of J2142−4420 is remarkably flat instead, at $\Gamma_{\rm X} = 1.06\ (\pm 0.14)$. The two spectra are shown in Fig. 2 with the best-fit power-law models, and illustrate how J2142−4420 is detected also below 1 keV at the 3.5σ level, ruling out the presence of a strong low-energy cut-off at $E < 4$ keV in the rest frame.

We also conducted another model fit by adding an additional parameter to account for any possible column density $N_{\rm H}(z)$ in the source frame, preserving the overall number of degrees of freedom by fixing the continuum photon index to $\Gamma_{\rm X} = 1.9$. The absorbed power-law model returns a nearly identical fit statistics for J2142−4419, and only an upper limit of $N_{\rm H}(z) < 1.0 \times 10^{22}$ cm^{-2} can be placed on the local column density. Conversely, for J2142−4420 the fit actually worsens by $\Delta C = 7$, as tilting the continuum slope from the intrinsic $\Gamma_{\rm X} = 1.9$ to the observed $\Gamma_{\rm X} \sim 1.1$ requires a column density $N_{\rm H}(z) \sim 1.6 \times 10^{23}$ cm^{-2}, which leaves clear positive residuals below 1 keV.

A simple absorption-based model therefore fails to reproduce the X-ray spectrum of J2142−4420.

Alternatively, one might suspect that the direct X-ray continuum from J2142−4420 is completely attenuated by a Compton-thick foreground screen, and that the observed emission is dominated by reflection from distant material. The latter interpretation is supported by a tentative line-like excess around 1.5–1.6 keV (which can be noticed in Fig. 2 despite the coarse binning), suggesting the presence of a Fe K feature (6.4–7 keV in the rest frame, depending on the ionization state). When an unresolved Gaussian profile is added to the baseline power-law model, the fit improves by $\Delta C = -11$ with the loss of two degrees of freedom. The line would have a rest energy of $E_{\rm K} = 6.8^{+0.1}_{-0.5}$ keV and a rest equivalent width of ~ 1 keV. This scenario, however, appears unlikely for the following reasons. First, reflection spectra from neutral matter are characterized by a much flatter continuum than observed here, if not inverted (i.e. $\Gamma_{\rm X} < 0$). Indeed, the spectrum of J2142−4420 can be accounted for by a reflection model that self-consistently includes continuum and emission lines (e.g. García et al. 2013) only allowing for a relatively high ionization of the gas, as also implied by the centroid energy of the putative Fe K feature. This poses several problems in terms of gas location and scattering geometry. Second, and even more importantly, the line-like excess is nearly coincident with one of the strongest features of the EPIC internal quiescent background, due to Al Kα fluorescence (e.g. Nevalainen, Markevitch & Lumb 2005).

We therefore believe that the ~ 1.6-keV line is an artefact associated with an imperfect background subtraction or calibration inaccuracies (or a combination of the two). Such a conclusion is corroborated by the fact that a similar feature, although with lower significance, seems to be present also in the spectrum of LBQS 2138−4427.[4] We finally note that, in the absence of a direct continuum, no sensible combination of reflected and scattered (e.g. Gupta et al. 2021, and references therein) emission can account for the observed spectral slope of J2142−4420, whose origin remains unclear. For completeness, we also analysed with the same approach the spectrum of LBQS 2138−4427. The X-ray properties of this source are similar to those of J2142−4420. The continuum is flat, with $\Gamma_{\rm X} = 1.11 \pm 0.17$, yet this time the absorbed power-law model results in a marginal statistical improvement ($\Delta C = -3$ for $\Gamma_{\rm X} = 1.9$), suggesting a local column of $N_{\rm H}(z) = 6^{+3}_{-2} \times 10^{22}$ cm^{-2}.

3.1 Source detection within and beyond the MUDF field

Given the presence of nearby point-like or extended (i.e. more than the *XMM–Newton* point spread function) emission structures in the MUDF, we searched for additional X-ray detections within the *F140W*/*HST* field of view. As the *XMM–Newton* field is far larger than the *F140W*/*HST* coverage, we extended this search to a distance of 10 arcmin to provide a detection list that roughly matches the distance of the quasar LBQS 2138−4427 from the MUDF field. We considered the centre of the MUDF/*HST* field at the coordinates (325.6, −44.33) degrees and we cross-matched them with the 4XMM–DR12 source catalogue (Webb et al. 2020). 4XMM–DR12 is the fourth generation catalogue of serendipitous X-ray sources available online and contains 939 270 X-ray source detections (630 347 unique X-ray sources) made public on or before 2021 December 31.[5] The net sky area covered when accounting for overlaps between observations is ∼1283 deg^2, for a net exposure time ≥1 ks. To define a reasonably clean sample, we have applied the following quality cuts from the 4XMM–DR12 catalogue: SUM_FLAG < 3 (low level of spurious detections), and CONFUSED = 0 (low probability of being associated with two or more distinct sources).[6] For the cross-match between the *HST*/MUDF and the 4XMM catalogues, we considered the corrected RA and Dec listed in the 4XMM catalogue after the application of a statistical correlation of the EMLDETECT coordinates with the USNO B1.0, 2MASS or SDSS (DR8) optical/IR source catalogues using the SAS task CATCORR (i.e. field rectification).[7] Therefore, the centroid is not necessarily the same as the one defined by the X-ray peak flux. This is also consistent with the source extraction performed by hand, as we considered the optical coordinates since the X-ray data are such that we cannot clearly identify the X-ray source position. The above search led to a sample of 119 X-ray detections, about 80 per cent of which are flagged as ‘good’ (94 detections with SUM_FLAG = 0, i.e. no warnings raised in any of the EPIC bands), whilst the remaining 25 detections have at least one warning flag raised, although the detection is considered reliable.

Inside the MUDF/*HST* field we found seven detections (see Fig. 3), three of which fall within the narrower MUSE field: J2142−4420 and J2142−4419 (although the identification with the latter is more controversial, see below), and a lower redshift quasar at $z \simeq 1.285$ (cyan cross in Fig. 8 by Fossati et al. 2019), which lies close to the edge of the MUSE FoV in close spatial proximity to a $z \simeq 0.67$ galaxy group (see Section 6.2 in Fossati et al. 2019 for more details). The low number of detected sources within the field is expected given the poorer *XMM–Newton* angular resolution (6 arcsec FWHM, or equivalently 15 arcsec half-energy width) as compared to *HST*.

Table 2 summarizes the properties of the seven X-ray detected sources within the *HST* field: the unique number (DETID), which identifies a detection as listed in the 4XMM–DR12 catalogue (column 1); RA and Dec relative to the X-ray position (columns 2 and 3); the observed flux with uncertainties in the 0.5–2 keV band (column 4), computed as the sum of the EPIC 0.5–1 and 1–2 keV energy bands (flagged in the catalogue as bands 2 and 3, respectively); the observed flux with uncertainties in the 2–12 keV band (column 5), computed as the sum of the EPIC 2–4.5 and 4.5–12 keV energy bands (flagged in the catalogue as band 4 and 5, respectively); the EPIC detection maximum likelihood (EP_8_DET_ML) value in the 0.2–12.0 keV band (column 6). We also included the *HST* catalogue IDs (column 7) for objects covered by the *F140W* and the redshift (column 8).

Of the seven X-ray detections within the *HST* field, only two have a single *HST* counterpart within 3 arcsec from the *XMM–Newton* location, i.e. SRC_NUM[8] = 56 and 83 (see Fig. 4). We do not have any spectral coverage for these two objects. SRC_NUM = 83 shows slightly extended emission as well as faint, possibly offset emission in *F336W*, so it could be either a star or another AGN, but the correct classification requires additional spectroscopy. The object with SRC_NUM = 56, located at the extreme edge of the *F140W* coverage, is a foreground Milky Way star (probably a Wolf-Rayet). Counterparts for the X-ray detections flagged with

---

[4] The spectrum of J2142−4419 is too faint to appreciate this effect.

[5] http://xmmssc.irap.omp.eu/Catalogue/4XMM-DR12/4XMM_DR12.html

[6] For more details, the interested reader should refer to the 4XMM catalogue user guide at the following website http://xmmssc.irap.omp.eu/Catalogue/4XMM-DR12/4XMM-DR12_Catalogue_User_Guide.html.

[7] http://xmmssc.irap.omp.eu/3XMM-DR4/UserGuide_xmmcat.html#Astrom

[8] The SRC_NUM represents the (decimal) source number in the individual source list for the relative *XMM–Newton* observation (i.e. the last digits of DETID).

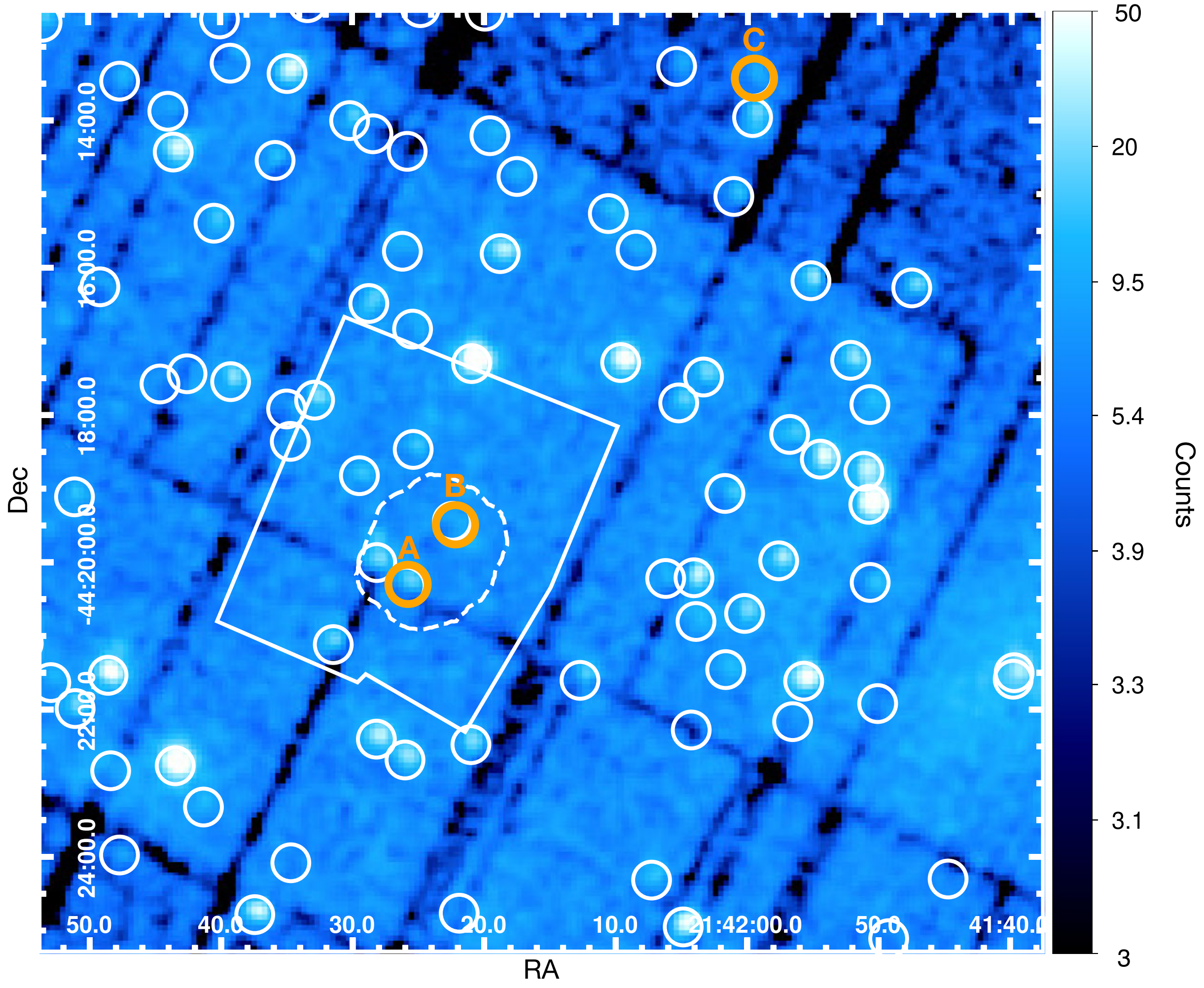

Figure 3. *XMM–Newton* 0.5–7 keV band mosaic of the pn, MOS1, and MOS2 detectors. The area marked with the white solid line represents the *F140W*/*HST* coverage. The white dashed lines marks the MUSE region with at least 4 h of exposure. Orange circles represent J2142−4420, J2142−4419, and LBQS 2138−4427. White circles mark detected sources within 10′ from the centre of the MUDF field. The image is spatially binned and smoothed through a Gaussian function. Labels A, B, and C as in Table 1. We have considered an intensity scaling between 3 and 50 X-ray counts to balance the contrast between faint and bright sources in the field.

Table 2. Summary of the properties of the seven X-ray detected sources (see Section 3.1 for details) within the *HST* field.

DETID[a]	RA	Dec	F_S [b] erg s^{-1} cm^{-2}	F_H [c] erg s^{-1} cm^{-2}	DETML[d]	*HST* ID[e]	redshift
108405501010054	325.617301	−44.333479	2.26 ± 0.23	15.10 ± 1.97	232	20 557	1.286
108405501010056	325.636933	−44.296718	2.98 ± 0.24	1.76 ± 0.97	204	2764	–
108405501010083	325.631084	−44.352039	2.06 ± 0.23	7.71 ± 1.82	110	273	–
108405501010091†	325.607981	−44.338811	1.57 ± 0.20	3.21 ± 1.08	79	20 405	3.223
108405501010122	325.622778	−44.313822	0.21 ± 0.10	8.46 ± 1.60	43	2268 + 2208	1.249
108405501010159	325.605758	−44.307890	0.58 ± 0.13	4.79 ± 1.46	31	2604	–
108405501010159	–	–	–	–	–	2606	–
108405501010159	–	–	–	–	–	2622	–
108405501010222††	325.593378	−44.324168	0.47 ± 0.13	0.35 ± 0.44	7	1535	3.230

Note. † J2142−4420. †† J2142−4419. [a] A unique number which identifies a detection listed in the 4XMM-DR12 catalogue. [b] EPIC flux in the 0.5–2 keV band (in units of 10^{-15} erg s^{-1} cm^{-2}). [c] EPIC flux in the 2–12 keV band (in units of 10^{-15} erg s^{-1} cm^{-2}). [d] EPIC detection maximum likelihood value in the 0.2–12.0 keV band. [e] *HST* ID as reported in the online catalogue published by Revalski et al. (2023).

SRC_NUM = 54, 91, 222, and 122 are, with different degrees of confidence, the $z \simeq 1.286$ quasar in close spatial proximity to a $z \simeq 0.67$ galaxy group, J2142−4420, J2142−4419, and another $z \simeq 1.249$ quasar, respectively, although the emission of the latter is closely blended with another *HST* object (*HST* ID=2208). In particular, the association of SRC_NUM = 222 with J2142−4419 is not straightforward, as several other optically detected sources lie closer to the coordinates of the X-ray detection. We recall that the

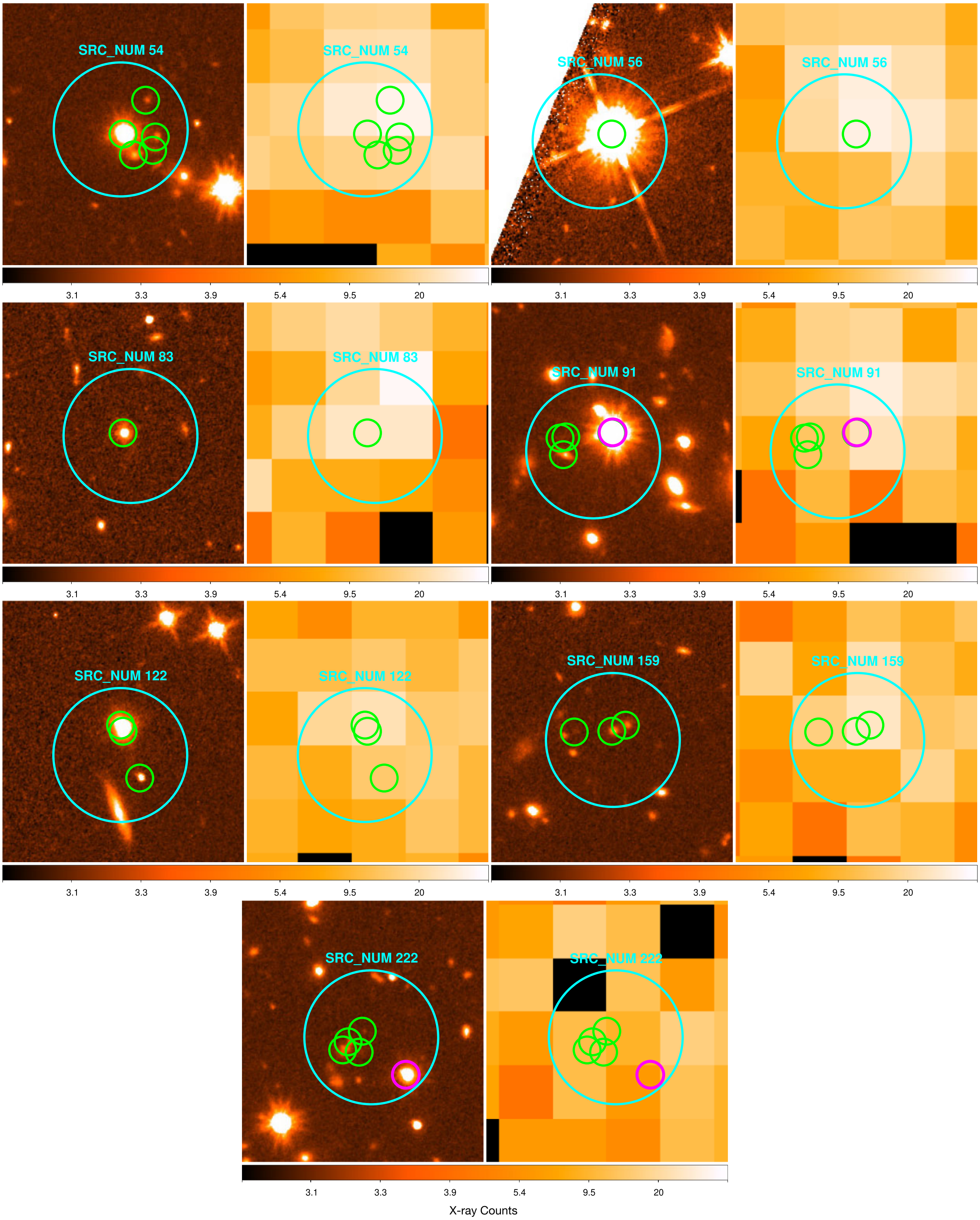

Figure 4. Cutouts displaying the seven X-ray detected sources within the *HST*/MUDF field. The *HST*/WFC3 *F140W* image is on the left while the *XMM–Newton* mosaic (pn, MOS1, and MOS2) in the 0.5–7 keV band is on the right. Each cutout has a size of ≃18 arcsec and it is centred at the *HST* location of the closest counterpart based on the distance separation between the *HST* and the *XMM–Newton* coordinates. In all the cutouts, the *XMM–Newton* position is marked by the cyan circle (5 arcsec radius, relative *XMM–Newton* astrometry is 1.5 arcsec at 1σ); the candidate counterpart(s) found within a 3 arcsec matching radius from the *XMM–Newton* position are shown with a green, 1 arcsec radius, circle. The two MUDF quasars are marked by a magenta circle. The common scale bar for each cutout is a logarithmic scale of the X-ray counts, with a minimum and maximum of 3 and 50, respectively. J2142−4420 can be safely associated with SRC_NUM = 91, while the identification of J2142−4419 with SRC_NUM = 222 is not straightforward (see text). The foreground $z \simeq 1.285$ quasar within the MUDF corresponds to SRC_NUM=54, although the field is rather crowded.

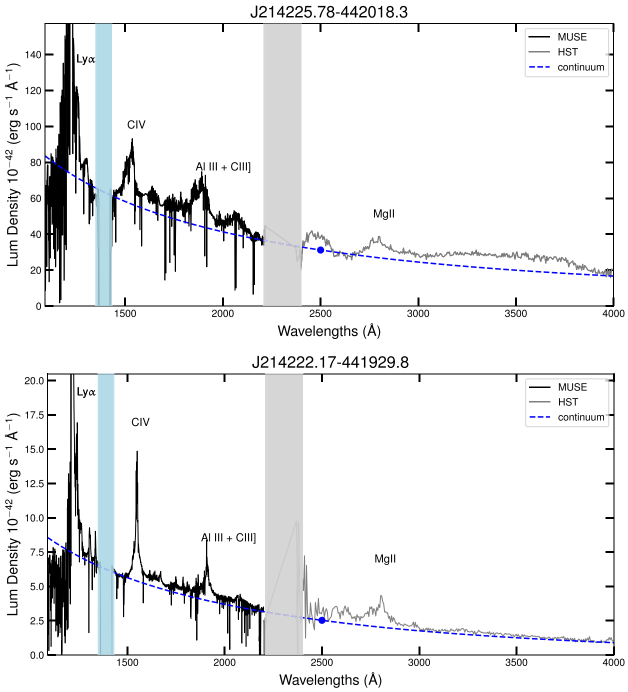

Figure 5. MUSE and *HST* spectra for the two quasars in the MUDF shown at rest wavelengths. The best-fit nuclear continuum is shown with the blue dashed line. All the other components considered in the spectral fit (e.g. iron complex) are not shown in this figure for visual clarity. The blue point marks the rest-frame continuum luminosity at 2500 Å. Grey shaded regions mask the gap between the MUSE and *HST* spectra, while the cyan shaded region masks the portion of the spectrum with missing data due to the blocking filter that avoids the light of the sodium laser of the adaptive optics system. The main emission lines are labelled.

spectral extraction region of 12 arcsec radius definitely encompasses any X-ray emission from J2142−4419, but it possibly includes also some contribution from these nearby objects. We therefore conclude that the X-ray fluxes we have derived for J2142−4419 from the spectral analysis, despite being already anomalously low, should be likely treated as upper limits. Depending on the actual level of contamination to its spectrum (Fig. 5), we cannot even exclude that J2142−4419 is heavily obscured in the X-rays. Subarcsecond accurate X-ray positions would be required to clarify this issue but, to date, no *Chandra* observations of the MUDF exist. Also for the remaining detection (SRC_NUM = 159), there is ambiguity on the most probable counterpart.

As a consistency check, we compared the flux values obtained for J2142−4420 and J2142−4419 from the spectral analysis with the catalogued ones. Based on the best-fit power-law model of J2142−4420 (Table 1), we obtain a flux of 8.2×10^{-15} erg s^{-1} cm^{-2} with statistical 1σ uncertainty of 18 per cent over the 0.3–7 keV band, while we have 1.6×10^{-15} erg s^{-1} cm^{-2} with 1σ uncertainty of ∼30 per cent for J2142−4419. These spectral fluxes are larger by factors of 1.5 (J2142−4420) and 1.1 (J2142−4419) than the catalogued values relative to the full EPIC band (0.2–12 keV, band 8). Given the large uncertainties, for J2142−4419, the agreement remains good (i.e. within 1σ) even after extrapolating the flux computed through our spectral analysis to the 0.2–12 keV EPIC band. For J2142−4420, instead, there is a formal inconsistency at the 2.2σ level with respect to the 4XMM catalogue, almost entirely arising above 2 keV. There are several possible explanations to alleviate this apparent discrepancy. Although we performed the spectral fits over the 0.3–7 keV energy range, almost no counts are detected beyond 5 keV for both quasars. Therefore, extrapolating the best-fit power law at higher energies (especially for a very flat Γ as found for J2142−4420) clearly leads to an overestimate of the hard-band flux. On the other hand, the catalogued band-8 fluxes for all the X-ray detected objects assume a fixed power-law source spectrum (Γ_X = 1.42; Webb et al. 2020) irrespective of the actual broad-band spectral shape. The EPIC total-band flux is then computed as the weighted average between the three detectors. This procedure, however, can introduce some systematic uncertainty at low fluxes. Indeed, the band-8 flux of J2142−4420 derived from the pn image is more than two times larger than those obtained from the MOS ones. This difference is entirely due to band 5 (4.5–12 keV), where no source counts are detected by either MOS camera, for a nominal zero flux. This brings down the combined EPIC band-5 (hence band-8) flux of J2142−4420. Incidentally, the catalogued band-8 pn flux for this quasar is 9.2×10^{-15} erg s^{-1} cm^{-2}, which is broadly consistent with our spectral estimate.

We finally note that, for a simple pivot effect, the above hard-band-related systematics have little impact on the determination of the monochromatic flux at rest-frame 2 keV. In fact, the fit anchors the continuum power law to the soft band, where most of the counts are found, so that the 2-keV flux is barely sensitive to the actual spectral slope. If anything, if we were to adopt the broad-band 4XMM fluxes as reference, both quasars would be even fainter in the X-rays than assumed in the following discussion, so our main results are completely unaffected.

4 ULTRAVIOLET SPECTRAL ANALYSIS

The MUSE and *HST* spectra are fitted by using the publicly available package for spectral fitting, `QSFit` (Calderone et al. 2017). The observed emission lines in quasar spectra are reproduced by a broad (FWHM > 2000 km s^{-1}) profile and, when required, an additional narrow component (FWHM < 2000 km s^{-1}) is included, while the continuum considers contributions from both the iron UV complex and the nuclear ionizing continuum (i.e. disc emission). To improve the residuals, we also considered a set of ‘unknown’ emission lines, i.e. emissions not associated with any known line (see Section 2.7 in Calderone et al. 2017). These components account for the lack of an iron template in the wavelength range 3100–3500 Å, or for possible asymmetric profiles in known emission lines. The spectra were corrected for Galactic extinction by using the $E(B-V)$ value of 0.017 from Schlafly & Finkbeiner (2011) and the parametrization by Cardelli, Clayton & Mathis (1989) and O’Donnell (1994), with a total to selective extinction parameter $R_V = 3.1$ (Calderone et al. 2017).

At rest-frame wavelengths bluer than ≃1216 Å, absorption from intergalactic H I attenuates the quasar flux, both in the Lyman series, and in the Lyman continuum (e.g. Prochaska, Worseck & O’Meara 2009). A correction for IGM absorption is thus required to properly retrieve both the Ly α and the continuum emission (e.g. Lusso et al. 2015). We also have a gap in the range 1362–1421 Å due to the blocking filter that avoids the light of the sodium laser of the adaptive optics system. Therefore, to perform the spectral fit, we conservatively neglected all the wavelengths shorter than 1450 Å at rest in the MUSE data.

The first few hundred angstroms of the *HST* spectrum are also neglected, as the extreme blue edge of the detector has some artefacts that produce erratic changes at the shortest wavelengths (i.e. around 2500 Å, see Fig. 5).

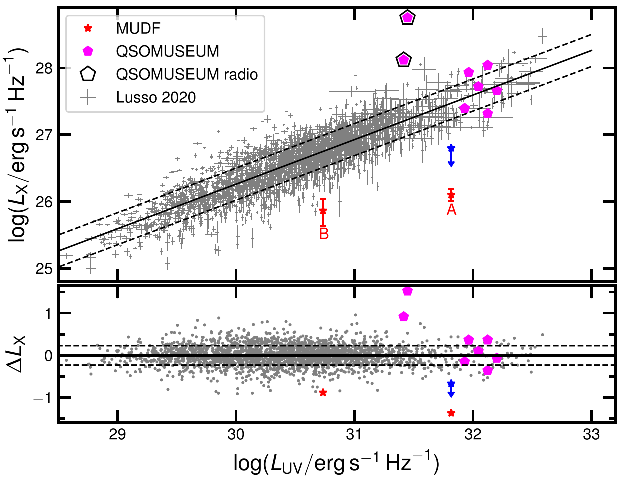

Figure 6. Rest-frame monochromatic luminosity at 2 keV (L_X) against the one at 2500 Å (L_{UV}) for the two quasars in the MUDF (red stars). The blue arrow represents the X-ray upper limit for J2142−4420 when an intrinsic column density is assumed (see Section 3 for details). The grey symbols represent the sample of ∼2400 quasars from Lusso et al. (2020), with the relative best-fit regression (black solid line). The dashed lines trace the 1σ dispersion, 0.24 dex. Magenta pentagons represent $z \simeq 3$ quasars from the QSO MUSEUM survey (Arrigoni Battaia et al. 2019a) with X-ray data available from the archive. Labels A and B as in Table 1.

Regarding the flux calibration, the MUSE detector has been extremely well calibrated over the last several years. Data have an absolute flux calibration accuracy of 5–10 per cent per single exposure, leading to uncertainties of a few per cent (dominated by systematics) on the final co-addition of several hundred exposures. Therefore, we adopted the MUSE data as a reference to match the *HST* spectra. On average, the *HST* and MUSE data are both well matched for all the sources observed in the MUDF, with flux differences within ∼10 per cent. Given the very few emission-line-free windows in the *HST* data, we prefer to adopt the same slope of the MUSE spectra for the *HST* data, although the slopes agree within uncertainties when fitted separately. Moreover, the MUSE and *HST* continuum levels were the same in the case of the brighter quasar, while an offset was applied to the *HST* data of J2142−4419 to better match the underlying MUSE continuum. This offset is none the less very small, less than a factor of 1.2 in flux. Fig. 5 presents the MUSE and *HST* spectra of the two quasars in the MUDF. Missing data in the MUSE spectrum is marked with a cyan-shaded region. Grey-shaded regions mask the gap between the MUSE and the *HST* spectra. The best-fit nuclear continuum is shown with the blue-dashed line ($\alpha_\nu = -0.67 \pm 0.05$ and $\alpha_\nu = -0.57 \pm 0.05$ for J2142−4420 and J2142−4419, respectively), while the blue point refers to the rest-frame continuum luminosity at 2500 Å.

5 RESULTS AND DISCUSSION

Fig. 6 shows the rest-frame monochromatic luminosity L_X against L_{UV} for the two quasars in the MUDF. The blue arrow is the X-ray flux for J2142−4420 when an intrinsic column density and a fixed $\Gamma_X = 1.9$ are assumed. We recall that the latter spectral fit is statistically worse than the case where no intrinsic absorption is allowed for (see Section 3 for details), yet we adopt the resulting X-ray flux as a conservative upper limit. Likewise, the flux of J2142−4419 should likely be considered as an upper limit due to the possible contamination from nearby objects (Section 3.1). Fig. 6 also shows the sample of quasars from Lusso et al. (2020), with the relative best-fit regression line (with a slope $\gamma = 0.667 \pm 0.007$ and intercept $\beta = 6.25 \pm 0.23$) for comparison. The dashed lines trace the 1σ dispersion, 0.24 dex. The Lusso et al. (2020) sample is composed by 2421 optically selected quasars (the majority from SDSS) with X-ray data from *XMM–Newton* and *Chandra*, and it spans a redshift range $0.01 \leq z \leq 7.54$, with a mean (median) redshift of 1.4 (1.3). These sources were selected to represent typical quasars, thus to have minimal host-galaxy contamination (especially important for the $z < 0.7$ AGN) and minimal gas and dust absorption. The Eddington bias is also taken into account. Details about the sample selection are provided in their Section 5.

From an observational perspective, the L_X–L_{UV} relationship provides a robust estimate of the quasar's expected X-ray luminosity for any given UV luminosity, thus determining the range of soft X-ray emission for typical (i.e. non-broad absorption line, non-jetted, with minimal dust and gas absorption) quasars or, vice versa, pinpointing peculiar objects (e.g. X-ray weak, with strong radio jets, or extremely red). Physically, this relation indicates a strong link between the accretion disc (emitting in the UV) and the X-ray corona (e.g. Tananbaum et al. 1979; Zamorani et al. 1981; Vignali, Brandt & Schneider 2003; Steffen et al. 2006; Just et al. 2007; Lusso et al. 2010; Martocchia et al. 2017). This non-linear correlation is tight ($\lesssim$0.24 dex of scatter; Lusso & Risaliti 2016), with a slope independent of redshift, suggesting that the connection between the disc and the corona must exist in AGN across cosmic time (e.g. Nicastro 2000; Merloni 2003; Lusso & Risaliti 2017; Arcodia et al. 2019).

Both J2142−4420 and J2142−4419 deviate from the L_X–L_{UV} relation, with faint X-rays with respect to quasars at similar UV luminosities. This is even more striking for J2142−4420, whose X-ray emission lies at $>3\sigma$ below the L_X–L_{UV} relation. This source shows an X-ray behaviour similar to the X-ray weak quasars at $z = 3.0$–3.3 published by Nardini et al. (2019), who discovered that ≈25 per cent of the quasars in their sample present an X-ray emission much weaker than expected, by factors of 3 or higher. Such an X-ray weak fraction is significantly larger than those previously reported for radio-quiet, non-broad absorption line (BAL) quasars at lower redshift and luminosity (≈8 per cent, e.g. Gibson, Brandt & Schneider 2008; Pu et al. 2020, see also Timlin et al. 2020a). Their X-ray weak quasars display a flat photon index ($\Gamma_X < 1.6$) with no clear evidence of X-ray absorption in the *XMM–Newton* spectra. The expected fluxes at rest-frame 2 keV, if the MUDF quasars were to follow the L_X–L_{UV} relationship published by Lusso et al. (2020), are listed in Table 1. The observed X-ray fluxes at 2 keV are fainter by a factor of ∼23.5 and 7.6 than the expectations for J2142–4420 and J2142–4419, respectively.

We also included in Fig. 6 all quasars within the QSO MUSEUM survey (Arrigoni Battaia et al. 2019a) with an X-ray observation available. The QSO MUSEUM (Quasar Snapshot Observations with MUse: Search for Extended Ultraviolet eMission) sample consists of 61 quasars at $3.03 < z < 3.46$ (median redshift $z = 3.17$) with absolute i-band magnitude normalized at $z = 2$ (Ross et al. 2013) in the range $-29.7 \leq M_i(z = 2) \leq -27.0$ and different strengths of radio emission. All these quasars have been observed with MUSE to characterize the physical properties of the CGM and IGM in emission (chiefly through the Lyα transition) associated to these bright quasars.

We have searched for any X-ray observations (either pointed or serendipitous) of all the QSO MUSEUM sources in the *XMM–Newton* and *Chandra* archives. Besides J2142−4420 and LBQS 2138−4427, which are also part of the sample, we found eight other objects with publicly available X-ray data. Two sources belong to

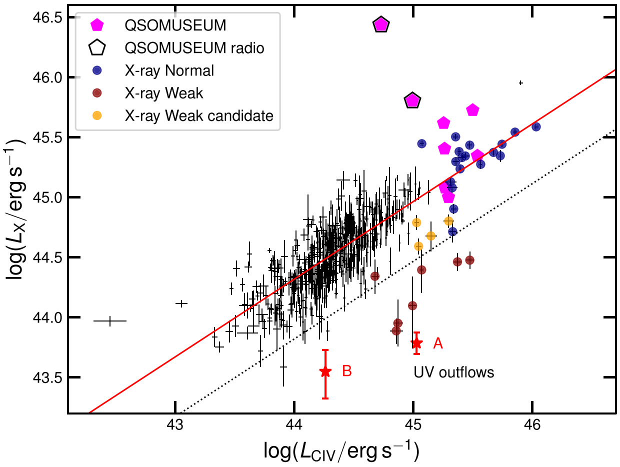

Figure 7. X-ray luminosity at rest-frame 2 keV as a function of the total integrated C IV line luminosity. Black symbols describe a sample of quasars with SDSS and XMM data at lower redshift and luminosity, with respect to the MUDF quasars, with a robust measurement of the integrated C IV line emission (Signorini et al., in preparation). The red solid line is the best-fit regression obtained with the SDSS-XMM sample and the X-ray Normal $z \simeq 3$ quasars. The dotted line is 3× the intrinsic dispersion on the best-fit relation, $\simeq$0.5 dex. Blue, brown, and orange symbols represent X-ray normal, weak and weak candidates, respectively, following the definition in Section 2.3 in Lusso et al. (2021). Red stars are J2142−4420 and J2142−4419. Magenta pentagons represent $z \simeq 3$ quasars from the QSO MUSEUM survey (Arrigoni Battaia et al. 2019a) with X-ray data available from the archive. Labels A and B as in Table 1.

the Nardini et al. (2019) sample, and are not re-analysed here. For the remaining six quasars, we retrieved and reduced the archival data with the standard procedures, and analysed the extracted spectra as described in Section 3. More details on the targets and on the observations are provided in Appendix A. Their rest-frame luminosities at 2500 Å are computed from the extrapolation of the continuum best fit of the MUSE spectra with a similar methodology as discussed in Section 4 (no *HST* data are available for this sample).

The majority of quasars lie in agreement with the $L_X - L_{UV}$ relation. ID49 and ID54 are bright radio sources therefore their X-ray emission includes an additional synchrotron component due to the radio jet. Only J2142−4420 (i.e. ID22) and J2142−4419 appear to be X-ray weak, leading to an X-ray weak fraction of 20 per cent, which raises to 25 per cent if we exclude the radio-bright quasars. Given the current data, we thus conclude that the fact that both quasars in the MUDF are X-ray weak is likely to be serendipitous and mostly driven by the higher probability to observe an X-ray weak quasar at these redshifts.

The MUDF quasars are located in the lower right corner of the L_X–$L_{\mathrm{C\,IV}}$ plane, as shown in Fig. 7, consistently to what is observed by Nardini et al. (2019) and Lusso et al. (2021) in their X-ray weak quasar sample. By analysing the properties of the high-ionization C IV λ1549 broad emission line in connection with the X-ray emission, Lusso et al. (2021) observed a tight correlation (with a slope of 0.647 ± 0.001 and an observed dispersion of $\simeq$0.2 dex), between the X-ray luminosity at rest-frame 2 keV and the total integrated C IV line luminosity (see their Fig. 14), in a sample of $\simeq$1800 quasars. Their sample was selected to fulfil all the quality criteria discussed by Lusso et al. (2020), thus non-broad absorption line, non-jetted, with minimal deviation due to absorption at both UV and X-rays, so it is representative of typical blue quasars in the redshift range $1.7 \lesssim z \lesssim 3.3$. The observed L_X–$L_{\mathrm{C\,IV}}$ relation implies a strong link between the relative strength of the X-rays with respect to both the UV continuum and the C IV line emission (see their Fig. 15, their Section 4.5 and relative discussion for more details). Trefoloni et al. (2023, see also Nardini et al. 2019; Lusso et al. 2021) argue that X-ray weakness could also be interpreted in a starved X-ray corona picture, connected with an ongoing wind phase that may extend to kpc scales (e.g. Bischetti et al. 2017; Vietri et al. 2018; Zappacosta et al. 2020; Temple et al. 2023, and references therein). If the wind is ejected in the vicinity of the black hole, the UV light that reaches the corona will be depleted, depriving the corona of seed photons and eventually generating an X-ray weak quasar. Yet, in the quasar luminosity regime, there will still be an ample reservoir of ionizing photons that produce the C IV emission observed in the X-ray weak quasars with respect to typical sources of similar X-ray luminosities (see Section 5 in Lusso et al. 2021).

We also note that the MUDF is not covered by any radio facility at present. We searched in the FIRST, NVSS, ALMA, NRAO (EVLA, GBT, GMVA, VLA, VLBA), and LOFAR archives, finding no matches, so we do not have any information regarding whether MUDF quasars are radio bright or not. Radio data may help in the interpretation of the X-ray data, since synchrotron emission may emit at X-ray energies as well (see e.g. Page et al. 2005; Zhu et al. 2020). Yet, since both MUDF quasars are X-ray weak, we may guess that they are also radio quiet, even accounting for possible X-ray variability. While possible X-ray obscuration of the coronal emission can occur at circumnuclear scales (broad-line region and/or torus), a Compton-thick column at host-galaxy scales would be required to fully absorb the emission of an extended jet, which seems highly unlikely.

Summarizing, we found that both MUDF quasars are intrinsically X-ray underluminous with respect to typical quasars at similar UV and C IV luminosities and redshifts. We do not know whether extreme X-ray variability (e.g. Timlin John D. et al. 2020b) may play a role, as multiple X-ray observations are not available, but this is very unlikely to occur *in phase* for both sources. We cannot thus exclude that the observed, simultaneous X-ray deficit could have instead a causal, common physical origin for both MUDF quasars. This might be related to the SMBH growth history (i.e. duty cycle), the environment, and/or the small-scale accretion physics of the two quasars, but we cannot investigate these scenarios any further at this stage, until more data are collected (e.g. deeper X-ray and radio observations). None the less, we found consistent results with previous works in the literature that observed a high fraction ($\sim$25 per cent) of X-ray weak quasars at $z \simeq 3$ (e.g. Nardini et al. 2019; Zappacosta et al. 2020; Lusso et al. 2021) with respect to lower redshift AGN samples ($\simeq$ 8 per cent, see e.g. Gibson et al. 2008; Pu et al. 2020; Timlin et al. 2020a). These works point towards a high incidence of outflowing gas in the X-ray weak population with respect to the X-ray normal one at high redshifts. Alternatively to starving the corona, such outflows could also provide an additional source of X-ray obscuration (e.g. Huang et al. 2023), although absorption does not clearly emerge from our spectral analysis.

5.1 The nebula-quasar connection

Mackenzie et al. (2021) found a statistically significant correlation between the surface brightness (SB) of the nebula observed in Lyα emission at the redshift of quasars and the luminosity of the quasar in both UV continuum and Lyα. Specifically, they observed that fainter quasars in the UV have on average smaller, less-luminous nebulae, with lower outer SBs (see their Fig. 6). They defined the size of a

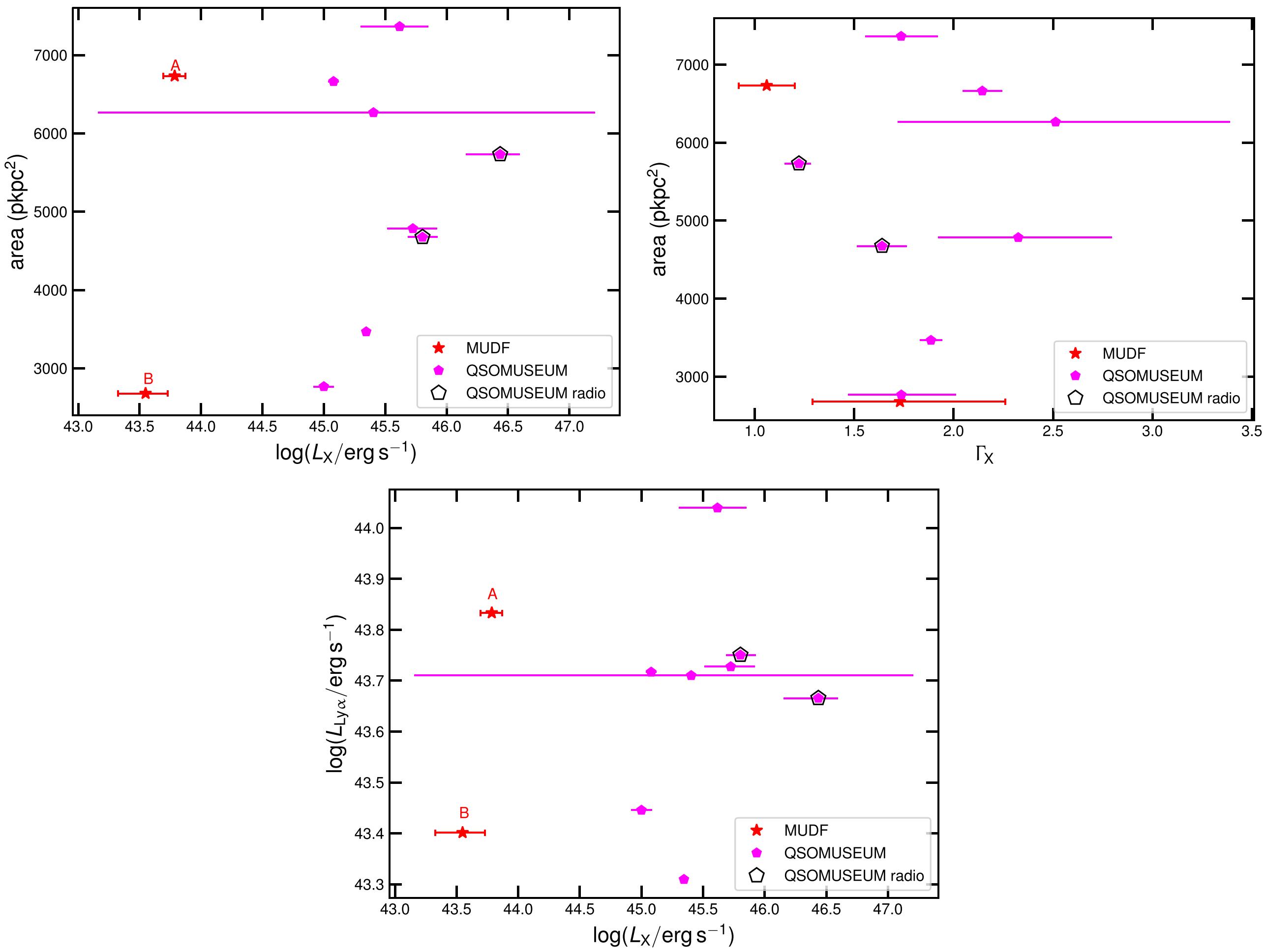

Figure 8. Upper left-hand panel: area of the extended Lyα emission as a function of the quasar luminosity at rest-frame 2 keV. Key symbols as in Fig. 6. The large error bars on L_X for ID27 take into account the large uncertainties on the photon index observed for that source (see Appendix A). Upper right-hand panel: area of the extended Lyα emission as a function of the X-ray photon index. Bottom panel: Lyα integrated emission as a function of the luminosity at rest-frame 2 keV. We note that the MUDF and QSO MUSEUM Lyα values have been computed under slightly different assumptions. Yet, the lack of a correlation holds even after accounting for minor systematics.

nebula as the largest projected distance (maximum extent) between pixels within the 3D mask of the optimally extracted MUSE images. This mask comprises all the voxels (volume pixels) identified as part of the Lyα nebulae, which are then used to define the size and properties of the nebulae (see their Section 3.1 for more details). This definition represents a good metric of the morphology of the nebulae only if the asymmetry in the extended Lyα emission is limited, which is often not the case (see e.g. Arrigoni Battaia et al. 2016; Borisova et al. 2016).

To quantify the scale of the nebulae, here we computed the area of the extended Lyα emission as the sum of pixels above a given Lyα SB level, which is less sensitive to possible asymmetries of the nebulae. To define a common SB value for both the MUDF and QSO MUSEUM data sets, we considered the shallowest MUSE datacube (i.e. ID21), finding a SB of 1.2×10^{-18} erg s^{-1} cm^{-2} arcsec^{-2} (at the 2σ statistical level) at $z = 3.218$, which we consider as a reference (SB$_{\rm ref}$). We then corrected this value for the cosmological dimming as $\mathrm{SB_{cut}} = \mathrm{SB_{ref}} \times (1 + z_{\rm ref})^4/(1 + z)^4$. For the bright MUDF quasar, J2142−4420, we obtain ∼114 arcsec^2, which translates into 6732 proper kpc^2 (with a conversion of ≃7.7 kpc per arcsec at $z = 3.22$). For J2142−4419, we obtain ∼45 arcsec^2, or equivalently 2679 proper kpc^2. This value may be slightly underestimated because of the presence of a bright star to the south of the nebula. Figs 8 and 9 present the area of the extended Lyα emission as a function of the nuclear luminosity at rest-frame 2 keV and 2500 Å. We do not observe any statistically significant correlation of the area with either of these two luminosities: small and large nebulae are equally distributed within a similar range of nuclear ionizing powers. The absence of a trend between area and nuclear luminosity is also confirmed if we exclude the X-ray weak and the two radio bright quasars. The area of the nebulae is also not correlated with the X-ray photon index, as shown in the upper right-hand panel of Fig. 8.

For completeness, we also considered whether there is any trend between the Lyα emission of the nebulae ($L_{\rm Ly\alpha}$) and the quasar rest-frame 2 keV luminosity, but we found none (Fig. 8). The luminosity values for the extended Lyα emission have been taken directly from the relevant papers (i.e. Table 1 in Lusso et al. 2019b and Table 2 in Arrigoni Battaia et al. 2019a). For the MUDF data, even if the field has now reached a much deeper MUSE exposure than that considered in the original work, the extended emission at the edge of the SB tails is negligible with respect to the total one. Therefore, the values for $L_{\rm Ly\alpha}$ have not changed significantly, even considering

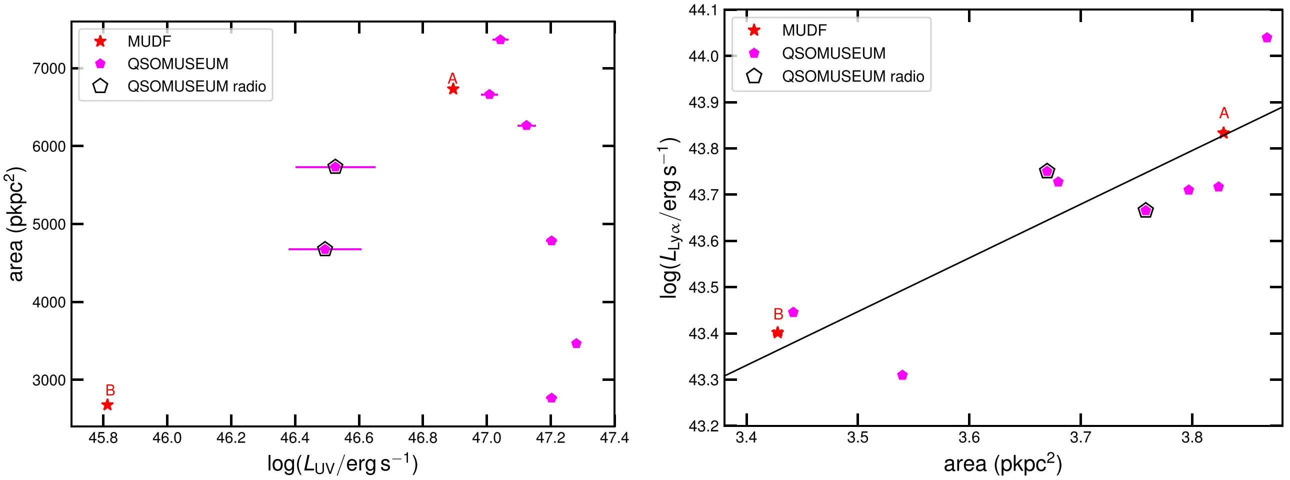

Figure 9. Left-hand panel: area of the extended Lyα emission as a function of the quasar luminosity at rest-frame 2500 Å. Right-hand panel: Lyα integrated emission as a function of the area. The MUDF and QSO MUSEUM Lyα values have been computed under slightly different assumptions, but any relative shifts are within the scatter of the relation (see Section 5.1 for details). The black solid line is the best regression fit of the sample.

the deeper data. The $L_{\rm Ly\alpha}$ values for the QSO MUSEUM sample have been computed by employing much shallower data instead. For the quasar in common between the MUDF and QSO MUSEUM (ID22, i.e. J2142−4420), the $L_{\rm Ly\alpha}$ value in the latter analysis is higher by a factor of ∼1.5 (in flux) than the one reported in Lusso et al. (2019b). This 0.2 dex difference is likely caused by the fact that, to identify the Lyα extended emission around the quasars, in the QSO MUSEUM analysis a minimum ‘volume’ of 1000 connected voxels above S/N >2 was considered, against 2500 connected voxels at S/N ≥ 2.5 in Lusso et al. (2019b). This implies that some noise could be included in the QSO MUSEUM flux measurements, but changing the thresholds would just introduce a systematic shift that does not change the main result, which is the absence of a trend between $L_{\rm Ly\alpha}$ and $L_{\rm X}$. Finally, Fig. 9 also shows the $L_{\rm Ly\alpha}$ integrated emission of the nebulae as a function of their area. These two quantities are correlated, with the area increasing with increasing Lyα emission, in broad agreement with what was found by Mackenzie et al. (2021). The best-fit regression line is

$$\log(L_{\rm Ly\alpha}/[10^{44}\,{\rm erg\,s^{-1}}]) = (1.16\pm0.06)\log({\rm area}/[{\rm pkpc^2}]) + (-4.42\pm0.77), \tag{1}$$

with a dispersion of 0.12 dex. The observed relation is in agreement with what found by Arrigoni Battaia et al. (2023, see their Table 1 for the resulting relationships with the physical area), who argue that host-galaxy inclination could be the main driver for the shape of the nebulae and their brightness, and thus for the relation itself (see their Section 5).

Overall, our results are qualitatively at odds with the interpretation by Mackenzie et al. (2021) that the quasar ionizing power is the main driver of the nebulae properties (i.e. luminosity and size; see also Renyue and Zheng 2013). Yet, given all the caveats discussed above, we caution that a one-to-one comparison of the sizes and areas with the luminosities measured in MUDF and QSO MUSEUM datacubes and other studies is not straightforward, because of the different sensitivity limits, techniques, and definitions of the extent of the diffuse Lyα emission. Additionally, the geometry of the host galaxy may also play a role (edge-on versus face-on), giving rise to different nebular morphologies (e.g. Costa et al. 2022; Arrigoni Battaia et al. 2023; Renyue and Zheng 2013). The absence of any correlation between the quasar and the nebular properties (if confirmed with larger samples), combined with the fact that there is a tight correlation between the emission of the nebulae and their size, imply that the main drivers of the extent of the nebulae could be host galaxy inclination and the physical properties of the environment, such as its density and radiation (assuming the emission is due to photoionization and perhaps scattering). While the quasars provide the main reservoir of ionizing photons (see the discussion in Section 4.1 in Mackenzie et al. 2021) that ultimately powers the nebulae, our results suggest that the actual extent of the diffuse emission and its morphology (e.g. asymmetries) seem to be the result of scattering processes in the CGM (e.g. Arrigoni Battaia et al. 2019a; Costa et al. 2022). As the fraction of X-ray emission to optical/UV is less than 1 per cent for both J2142−4420 and J2142−4419 (see appendix C), this implies that the X-ray emission is not contributing significantly to the overall photon budget. We caution, however, that this fraction is computed by assuming that the X-ray emission that illuminates the Lyα nebulae of the MUDF quasars is the same as observed.

6 CONCLUSIONS

We present *XMM–Newton* observations of the MUSE Ultra Deep Field (MUDF), a unique region of the sky that hosts two quasars at $z \simeq 3.22$ with close separation (∼500 kpc). Observations at high energy characterize the innermost region of these quasars with physically associated extended Lyα nebulae, and provide imaging of the MUDF and the environment of this pair at much larger scales than those covered by either MUSE or *HST*. Thus, MUSE+*XMM–Newton* observations represent the first view of the assembly of a potentially massive $z \simeq 3.2$ overdensity. We searched for additional X-ray detections within the *F140W*/*HST* field of view around the MUDF. We extended this search to a distance of 10 arcmin to provide a detection list that roughly matches the distance of the third $z \sim 3.2$ quasar LBQS 21384427. We find 119 X-ray detections, with seven detections inside the MUDF/*HST* field. The three already known quasars (i.e. J2142−4420, J2142−4419, and a lower redshift quasar in close spatial proximity to a foreground $z \simeq 0.67$ galaxy group) within the MUSE coverage are all detected. These sources are the only ones detected within the MUSE footprint. For the additional sources in the *HST* field, only one has an ambiguous counterpart (SRC_NUM = 159), for which a subarcsecond-accurate X-ray position is required. Given the richness of the *HST* field, the *Chandra* subarcsecond spatial resolution and low background are essential to further disentangle multiple sources that are blurred in the large *XMM–Newton* point-spread function.

We find that both quasars in the MUDF are X-ray weak, outliers of the L_X–L_{UV} relation, with a C IV line emission in agreement with other X-ray weak quasars in the literature at $z \simeq 3$ and matching UV luminosities. This result is compatible with the higher probability to observe an X-ray weak quasar at these redshifts, as suggested by previous works analysing quasar samples at similar redshift and UV luminosities (e.g. Nardini et al. 2019; Zappacosta et al. 2020), and it might be interpreted in a starved X-ray corona scheme associated with an ongoing wind phase. If the wind starts off in the vicinity of the supermassive black hole, the accretion rate – and thus the UV light that reaches the X-ray corona – will diminish, depriving the hot coronal plasma of seed photons and resulting in an X-ray weak quasar. Yet, at high-UV luminosities there will still be sufficient ionizing photons to produce a strong C IV line emission as detected in X-ray weak quasars, which have higher $L_{\rm IV}$ compared to normal quasars at similar X-ray luminosities (Lusso et al. 2021; Trefoloni et al. 2023).

We do not observe any trend between the area of the Lyα nebulae and nuclear luminosities at either the rest-frame 2 keV or 2500 Å. The area of the nebulae is not correlated with the X-ray photon index nor with the integrated band flux in the hard band (2–10 keV). Quasars with similar luminosities can have very diverse Lyα areas. The absence of a relation between the extent of the nebula and the quasar ionizing power is at variance with what is observed by Mackenzie et al. (2021), who found a correlation between the size of the nebula (defined as the maximum extent) and the luminosity of the quasar in both UV continuum and Lyα. We also do not find any statistically significant trend between $L_{{\rm Ly}\alpha}$ and L_X. Finally, the MUDF quasars are in agreement with the relation between the $L_{{\rm Ly}\alpha}$ integrated emission of the nebulae and their area recently published by Arrigoni Battaia et al. (2023), suggesting that host-galaxy inclination could be among the main drivers for the morphology and brightness of the nebulae. However, a direct comparison of the sizes and areas with luminosities between different studies is challenging due to, e.g. different sample statistics, sensitivity limits, techniques, and definition of the extent of the diffuse Lyα emission). Our findings, if confirmed with larger samples, suggest that the nebular morphology is mainly driven by the physical properties of the environment in the host galaxy (e.g. geometry, density, temperature, column density, and filling factor or clumpiness), rather than the quasar power.

ACKNOWLEDGEMENTS

We thank the anonymous reviewer for their thorough reading and for useful comments and suggestions that have improved the clarity of the paper. EL acknowledges the support by the Fondazione Cassa di Risparmio Firenze (grant No 45780). SC acknowledges financial support of the Italian Ministry of Education, University, and Research with PRIN 201278X4FL and the 'Progetti Premiali' funding scheme. PD acknowledges support from the NWO grant 016.VIDI.189.162 ('ODIN') and from the European Commission's and University of Groningen's CO-FUND Rosalind Franklin program. Based on observations with the NASA/ESA *Hubble Space Telescope* obtained from the MAST Data Archive at the Space Telescope Science Institute, which is operated by the Association of Universities for Research in Astronomy, Incorporated, under NASA contract NAS5-26555. Support for program numbers 15637 and 15968 was provided through a grant from the STScI under NASA contract NAS5-26555. These observations are associated with program numbers 6631, 15637, and 15968. The MUSE portion of this project has received funding from the European Research Council (ERC) under the European Union's Horizon 2020 research and innovation program (grant agreement No 757535) and by Fondazione Cariplo (grant No 2018–2329).

DATA AVAILABILITY

Raw X-ray data are available via the *XMM–Newton* Science Archive (XSA). The processed *HST* and *XMM–Newton* observations are available at https://archive.stsci.edu/hlsp/mudf: (doi:10.17909/81fp-2g44).

REFERENCES

Anderson L. et al., 2014, MNRAS, 441, 24

Arcodia R., Merloni A., Nandra K., Ponti G., 2019, A&A, 628, A135

Arnaud K. A., 1996, in Jacoby G. H., Barnes J., eds, ASP Conf. Ser. Vol. 101, Astronomical Data Analysis Software and Systems V. Astron. Soc. Pac., San Francisco, 17

Arrigoni Battaia F. et al., 2019b, A&A, 631, A18

Arrigoni Battaia F., Hennawi J. F., Cantalupo S., Prochaska J. X., 2016, ApJ, 829, 3

Arrigoni Battaia F., Hennawi J. F., Prochaska J. X., Oñorbe J., Farina E. P., Cantalupo S., Lusso E., 2019a, MNRAS, 482, 3162

Arrigoni Battaia F., Obreja A., Costa T., Farina E. P., Cai Z., 2023, ApJ, 952, L24

Arrigoni Battaia F., Prochaska J. X., Hennawi J. F., Obreja A., Buck T., Cantalupo S., Dutton A. A., Macciò A. V., 2018, MNRAS, 473, 3907

Bacon R. et al., 2010, in McLean, Ian s., Ramsay, Suzanne K., Takami, Hideki, eds, Ground-based and Airborne Instrumentation for Astronomy III. vol 7735, Proceedings of the SPIE . p. 773508

Bacon R. et al., 2021, A&A, 647, A107

Basu-Zych A., Scharf C., 2004, ApJ, 615, L85

Bischetti M. et al., 2017, A&A, 598, A122

Bond J. R., Kofman L., Pogosyan D., 1996, Nature, 380, 603

Borisova E. et al., 2016, ApJ, 831, 39

Cai Z. et al., 2019, ApJS, 245, 23

Calderone G., Nicastro L., Ghisellini G., Dotti M., Sbarrato T., Shankar F., Colpi M., 2017, MNRAS, 472, 4051

Cantalupo S., 2017, in Fox A., Davé R., eds, Astrophysics and Space Science Library Vol. 430, Gas Accretion onto Galaxies. Springer International Publishing , p. 195

Cantalupo S., Arrigoni-Battaia F., Prochaska J. X., Hennawi J. F., Madau P., 2014, Nature, 506, 63

Cardelli J. A., Clayton G. C., Mathis J. S., 1989, ApJ, 345, 245

Cash W., 1979, ApJ, 228, 939

Chapman S. C., Lewis G. F., Scott D., Richards E., Borys C., Steidel C. C., Adelberger K. L., Shapley A. E., 2001, ApJ, 548, L17

Chapman S. C., Scott D., Windhorst R. A., Frayer D. T., Borys C., Lewis G. F., Ivison R. J., 2004, ApJ, 606, 85

Costa T., Arrigoni Battaia F., Farina E. P., Keating L. C., Rosdahl J., Kimm T., 2022, MNRAS, 517, 1767

D'Odorico V., Petitjean P., Cristiani S., 2002, A&A, 390, 13

Dayal P., Ferrara A., 2018, Phys. Rep., 780, 1

Dekker H., D'Odorico S., Kaufer A., Delabre B., Kotzlowski H., 2000, in Iye M., Moorwood A. F., eds, SPIE Conf. Ser. 4008, Optical and IR Telescope Instrumentation and Detectors. Society of Photo-Optical Instrumentation Engineers (SPIE) Conference Series Vol. 4008. SPIE, Bellingham, 534

Farina E. P. et al., 2019, ApJ, 887, 196

Fossati M. et al., 2019, MNRAS, 490, 1451

Fossati M. et al., 2021, MNRAS, 503, 3044

Francis P. J., Hewett P. C., 1993, AJ, 105, 1633

García J., Dauser T., Reynolds C. S., Kallman T. R., McClintock J. E., Wilms J., Eikmann W., 2013, ApJ, 768, 146
Geach J. E. et al., 2005, MNRAS, 363, 1398
Geach J. E. et al., 2009, ApJ, 700, 1
Gibson R. R., Brandt W. N., Schneider D. P., 2008, ApJ, 685, 773
Gupta K. K. et al., 2021, MNRAS, 504, 428
Hennawi J. F., Prochaska J. X., Cantalupo S., Arrigoni-Battaia F., 2015, Science, 348, 779
HI4PI Collaboration et al., 2016, A&A, 594, A116
Huang J. et al., 2023, ApJ, 950, 18
Just D. W., Brandt W. N., Shemmer O., Steffen A. T., Schneider D. P., Chartas G., Garmire G. P., 2007, ApJ, 665, 1004
Kaastra J. S., 2017, A&A, 605, A51
Kawamuro T., Schirmer M., Turner J. E. H., Davies R. L., Ichikawa K., 2017, ApJ, 848, 42
Kusakabe H. et al., 2022, A&A, 660, A44
Leclercq F. et al., 2017, A&A, 608, A8
Lehmer B. D. et al., 2009, ApJ, 691, 687
Lilly S. J., Cowie L. L., Gardner J. P., 1991, ApJ, 369, 79
Lujan Niemeyer M. et al., 2022, ApJ, 934, L26
Lusso E. et al., 2010, A&A, 512, A34
Lusso E. et al., 2013, ApJ, 777, 86
Lusso E. et al., 2019a, MNRAS, 485, L62
Lusso E. et al., 2020, A&A, 642, A150
Lusso E. et al., 2021, A&A, 653, A158
Lusso E., Piedipalumbo E., Risaliti G., Paolillo M., Bisogni S., Nardini E., Amati L., 2019b, A&A, 628, L4
Lusso E., Risaliti G., 2016, ApJ, 819, 154
Lusso E., Risaliti G., 2017, A&A, 602, A79
Lusso E., Worseck G., Hennawi J. F., Prochaska J. X., Vignali C., Stern J., O'Meara J. M., 2015, MNRAS, 449, 4204
Mackenzie R. et al., 2021, MNRAS, 502, 494
Malavasi N., Aghanim N., Douspis M., Tanimura H., Bonjean V., 2020, A&A, 642, A19
Martocchia S. et al., 2017, A&A, 608, A51
Matsuda Y. et al., 2004, AJ, 128, 569
McDonald P. et al., 2005, ApJ, 635, 761
Merloni A., 2003, MNRAS, 341, 1051
Monson E. B. et al., 2023, ApJ, 951, 15
Morrissey P. et al., 2018, ApJ, 864, 93
Nardini E. et al., 2019, A&A, 632, A109
Nevalainen J., Markevitch M., Lumb D., 2005, ApJ, 629, 172
Nicastro F., 2000, ApJ, 530, L65
Nilsson K. K., Fynbo J. P. U., Møller P., Sommer-Larsen J., Ledoux C., 2006, A&A, 452, L23
O'Donnell J. E., 1994, ApJ, 422, 158
O'Sullivan D. B., Martin C., Matuszewski M., Hoadley K., Hamden E., Neill J. D., Lin Z., Parihar P., 2020, ApJ, 894, 3
Page K. L., Reeves J. N., O'Brien P. T., Turner M. J. L., 2005, MNRAS, 364, 195
Prescott M. K. M., Momcheva I., Brammer G. B., Fynbo J. P. U., Møller P., 2015, ApJ, 802, 32
Prochaska J. X., Worseck G., O'Meara J. M., 2009, ApJ, 705, L113
Pu X., Luo B., Brandt W. N., Timlin J. D., Liu H., Ni Q., Wu J., 2020, ApJ, 900, 141
Reid B. A. et al., 2012, MNRAS, 426, 2719
Renyue C., Zheng Z., 2013, ApJ , 775, 112
Revalski M. et al., 2023, ApJS, 265, 40
Ross N. P. et al., 2013, ApJ, 773, 14
Sanderson K. N., Prescott M. K. M., Christensen L., Fynbo J., Møller P., 2021, ApJ, 923, 252
Schirmer M. et al., 2016, MNRAS, 463, 1554
Schlafly E. F., Finkbeiner D. P., 2011, ApJ, 737, 103
Scott A. E., Stewart G. C., Mateos S., Alexand er D. M., Hutton S., Ward M. J., 2011, MNRAS, 417, 992
Shang Z. et al., 2011, ApJS, 196, 2
Steffen A. T., Strateva I., Brandt W. N., Alexander D. M., Koekemoer A. M., Lehmer B. D., Schneider D. P., Vignali C., 2006, AJ, 131, 2826
Steidel C. C., Adelberger K. L., Dickinson M., Giavalisco M., Pettini M., Kellogg M., 1998, ApJ, 492, 428
Steidel C. C., Pettini M., Adelberger K. L., 2001, ApJ, 546, 665
Strüder L. et al., 2001, A&A, 365, L18
Tananbaum H. et al., 1979, ApJ, 234, L9
Temple M. J. et al., 2023, MNRAS, 523, 646
Timlin J. D. III, Brandt W. N., Zhu S., Liu H., Luo B., Ni Q., 2020b, MNRAS, 498, 4033
Timlin J. D., Brandt W. N., Ni Q., Luo B., Pu X., Schneider D. P., Vivek M., Yi W., 2020a, MNRAS, 492, 719
Trefoloni B. et al., 2023, preprint (arXiv:2305.07699)
Turner M. J. L. et al., 2001, A&A, 365, L27
Umehata H. et al., 2019, Science, 366, 97
Vietri G. et al., 2018, A&A, 617, A81
Vignali C., Brandt W. N., Schneider D. P., 2003, AJ, 125, 433
Webb N. A. et al., 2020, A&A, 641, A136
Wisotzki L. et al., 2018, Nature, 562, 229
Young M., Elvis M., Risaliti G., 2009, ApJS, 183, 17
Zamorani G. et al., 1981, ApJ, 245, 357
Zappacosta L. et al., 2020, A&A, 635, L5
Zhu S. F., Brandt W. N., Luo B., Wu J., Xue Y. Q., Yang G., 2020, MNRAS, 496, 245

APPENDIX A: X-RAY OBSERVATIONS OF QSO MUSEUM

As mentioned in the main text, neglecting J2142−4420 and LBQS 2138−4427 (ID22 and ID23, respectively), other eight out of the 61 sources in the QSO MUSEUM sample (Arrigoni Battaia et al. 2019a) have been observed in the X-rays by *XMM–Newton* and/or *Chandra*. We list below the observations that have been considered in this work. For each target, the key properties relevant to the present discussion, including those inferred from the X-ray analysis, are summarized in Table A1.

(i) QSO B0114−0857 was serendipitously observed by *Chandra* on 2020 October 16 and two days later, for a cumulative exposure of 37.7 ks. The source lies about 3 arcmin off-axis, and the spectra were extracted from a circular region with a radius of 5 arcsec. The analysis was carried out simultaneously on the two data sets, and the spectral fits were performed over the 0.6–6 keV band, where 74 (± 9) net counts are collected.

(ii) QSO B0537−286 was targeted several times, first by *XMM–Newton* on 2000 March 19, with net exposures of 19.4 ks for the pn and 38.8 ks for both MOS cameras. Another observation was performed on 2005 March 20. Neglecting a short snapshot on the same day, the on-source times are 31.8, 51.0, and 49.7 ks for pn, MOS1, and MOS2, respectively. The spectra were extracted from circular regions with radii of 35 (30) arcsec in the first (second) epoch for all the detectors. No exposure is affected by significant background flares, and about 31 and 45 kilo-counts are available over the entire 0.3–10 keV EPIC band. In between the two *XMM–Newton* visits, QSO B0537−286 was also observed by *Chandra* on 2003 July 21 for 30 ks. The extraction region is 8 arcsec wide as the source is >5 arcmin away from the nominal aimpoint and PSF distortion effects are non-negligible. The spectral analysis was performed over the 0.5–7 keV band, where ∼3600 counts were collected with a 0.1 per cent background level. In order to take into account the source variability, we considered in the plot the average flux of these three observations, while the error covers the min-to-max flux range.

(iii) SDSS J094734.19+142116.9 is part of the sample of luminous blue quasars at $z \simeq 3$ with pointed *XMM–Newton* observations discussed by Nardini et al. (2019). The source was observed on 2017 April 28, with good-time exposures of 24.2 ks (pn), 30.1 ks (MOS1),

Table A1. Properties of the QSO MUSEUM sources with X-ray observations.

Object	$z_{\rm sys}$ [a]	ID	C/ν	$\Gamma_{\rm X}$	$\log(\nu F_\nu)_{2\,\rm keV}$ [b] erg s^{-1} cm^{-2}	$L^c_{\rm UV}$ erg s^{-1} Hz^{-1}	$(\nu L_\nu)^d_{\rm CIV}$ erg s^{-1}	Area pkpc^2
QSO B0114−0857	3.204	31	55/65	1.737 (1.468, 2.011)	−13.96 (−14.04, −13.87)	1.33 ± 0.05	1973.0 ± 76.2	2767
QSO B0537−286	3.139	49	5757/6344	1.274 (1.266, 1.282)	−12.48 (−12.48, −12.47)	0.28 ± 0.07	536.6 ± 16.3	5732
	–		4598/4639	1.157 (1.150, 1.163)	−12.35 (−12.35, −12.34)	–	–	–
	–		404/425	1.236 (1.208, 1.264)	−12.76 (−12.78, −12.74)	–	–	–
SDSS J0947+1421	3.039	6	643/680	2.325 (1.921, 2.796)	−13.56 (−13.58, −13.53)	1.59 ± 0.04	3451.7 ± 121.5	3467
QSO J0958+1202	3.306	9	8/21	1.640 (1.513, 1.765)	−13.26 (−13.48, −13.07)	1.33 ± 0.05	3151.6 ± 105.7	4784
7C 1013+2053	3.108	54	113/132	1.736 (1.555, 1.921)	−13.12 (−13.24, −12.10)	0.26 ± 0.06	984.1 ± 18.7	4675
LBQS 1244+1129	3.155	59	449/504	–	−13.86 (−13.90, −13.82)	0.85 ± 0.05	1849.0 ± 48.9	6663
CTQ 669	3.219	21	129/137	2.513 (1.718, 3.388)	−13.34 (−13.66, −13.11)	0.92 ± 0.05	1797.4 ± 58.9	7364
QSO B2348−404	3.332	27	11/15	–	−13.59 (−15.84, −15.40)	1.11 ± 0.07	1828.7 ± 73.4	6265

Note. Values within the parenthesis represent the minimum and maximum value of the correspondent parameter. [a] Redshifts are obtained from the peak of the Lyα emission in the quasar spectrum (from Arrigoni Battaia et al. 2019a). [b] Flux at rest-frame 2 keV. [c] Monochromatic continuum luminosity at rest-frame 2500 Å normalized to 10^{32} erg s^{-1} Hz^{-1}. [d] Integrated C IV luminosity normalized to 10^{42} erg s^{-1}.

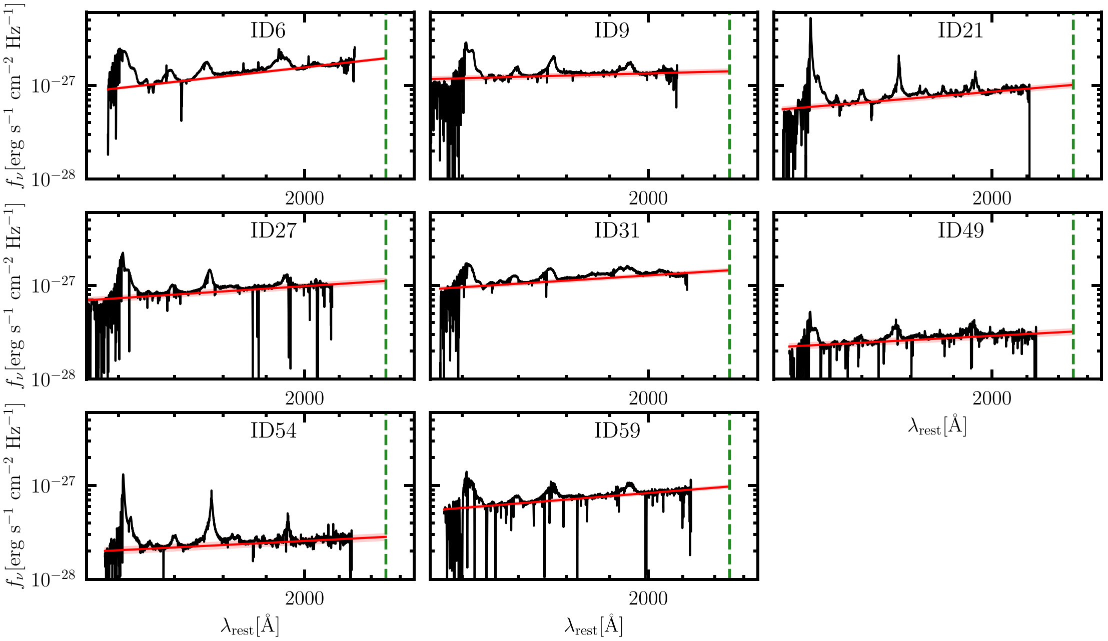

Figure A1. MUSE spectra of the eight quasars with X-ray archival data in the QSO MUSEUM sample. The red solid line represents the continuum (along with uncertainties in light red). The dashed line marks the 2500 Å wavelength at rest. All panels have the same ranges on both axes to ease comparison. The source ID (as listed in Arrigoni Battaia et al. 2019a) is shown at the top of each panel.

and 30.0 ks (MOS2). Over 1000 net counts were cumulatively obtained by the three EPIC detectors. The relevant X-ray properties have been directly retrieved from the spectral analysis of Nardini et al. (2019). An earlier *Chandra* snapshot (1.6 ks) provides much looser constraints and is neglected.

(iv) QSO J0958+1202 can instead rely only on one such *Chandra* observation, performed on 2012 April 22. Despite the short exposure (1.6 ks), the source is robustly detected, with 21 counts at 0.5–7 keV within a radius of 3 arcsec (estimated background 0.06), allowing a basic spectral analysis.

(v) 7C 1013+2053 was observed by *Chandra* on 2018 January 24 for 10 ks. The spectrum was extracted from a circular region with radius of 3 arcsec, and the source and estimated background counts in the 0.5–7 keV band are, respectively, 205 and ∼ 0.4.

(vi) LBQS 1244+1129 is also included in the study by Nardini et al. (2019), to which we refer for the details on the spectral analysis. The *XMM–Newton* observation took place on 2017 July 03, with exposures of 32.6 ks for the pn and 38.5 ks for both MOS cameras. About 560 source counts were collected at 0.5–8 keV.

(vii) CTQ 669 was serendipitously observed by *XMM–Newton* on 2011 October 11, with exposures of 8.8 ks for the pn and 11.5 ks for both MOS detectors. The spectra were extracted from circular regions with radius of 20 arcsec, with 112 (± 14) source counts at 0.3–8 keV. The pn spectrum, however, turned out to be inconsistent with the two MOS ones in terms of intensity, being brighter by about a factor of 3. A similar effect is noticed also in the relative fluxes of the three EPIC instruments reported in the latest *XMM–Newton* catalogue (4XMM–DR12; Webb et al. 2020) of serendipitous X-ray sources, and its origin is unclear. The observation is not affected by background flares, so a possible explanation could be the proximity of the target to the edge of the chip in the pn field of view, which might result in some problem with the effective-area correction in the auxiliary response file. We conservatively assumed the average flux of the pn and MOS observations, while the error is the half-difference between the two values.

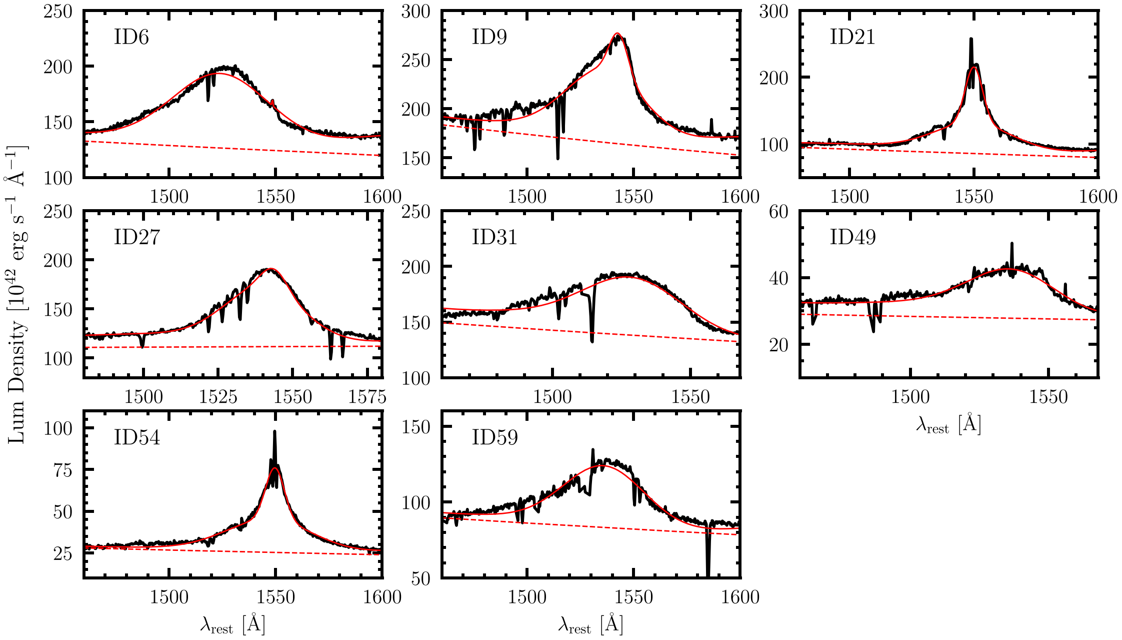

Figure A2. Fits to the C IV emission line of the 8 MUSE quasar spectra in the QSO MUSEUM sample with X-ray archival data. The spectra are shown with a black line, the best-fitting model in red, and the continuum with the red dashed line.

(viii) QSO B2348−404 was serendipitously observed by *XMM–Newton* on 2017 May 14, and is marginally detected in 4.4 ks only with the pn with ∼15 counts at 0.3–5 keV. The source is not detected with MOS1, and falls outside the MOS2 field of view.

APPENDIX B: ULTRAVIOLET OBSERVATIONS OF QSO MUSEUM

Figs A1 and A2 present the fit of the MUSE spectra of the eight quasars with X-ray archival data in the QSO MUSEUM sample. The flux, along with its uncertainty, at rest-frame 2500 Å has been obtained from the extrapolated best-fit continuum.

APPENDIX C: SPECTRAL ENERGY DISTRIBUTIONS OF THE MUDF $z \simeq 3$ QUASARS

For completeness, we also compiled the broad-band photometric SEDs, from the near-infrared to the X-rays, for the two MUDF quasars (Fig. C1). J2142−4420 has a rather good photometric coverage, from the rest-frame near-infrared with WISE (with a S/N > 3) and 2MASS, to the optical/UV with *HST* (*F140W*, *F125W*, *F702W*, *F450W*, *F336W*, see Revalski et al. 2023 for details), for a total of 12 photometric data points. J2142−4419 is instead detected in WISE/W1 and W2 (with a S/N > 2) only, but not in 2MASS. Together with the *HST* photometry, the rest-frame near-infrared to optical/UV SED has seven data points. The X-ray data are also included that have been corrected for Galactic absorption. Following a simplified approach as in Lusso et al. (2013, see their Section 4.2), we computed the bolometric luminosity as the integrated emission from 1 μm up to 1 keV,[9] as the quasar emission below and above this range is considered to be reprocessed. We find $L_{\rm bol} \simeq 2 \times 10^{47}$ and 2×10^{46} erg s^{-1} for J2142−4420 and J2142−4419, respectively. As the rest-frame 2–10 keV luminosity is 2.3×10^{44} and 7.2×10^{43} for the brighter and the fainter quasar in MUDF, we obtain an X-ray-to-optical/UV ratio less than 1 per cent for both sources, thus implying that the X-ray emission is a negligible fraction of the total one for the two MUDF quasars.

---

[9] The monochromatic luminosity at the rest-frame energy of 1 keV is about 3×10^{45} erg s^{-1} for both quasars.

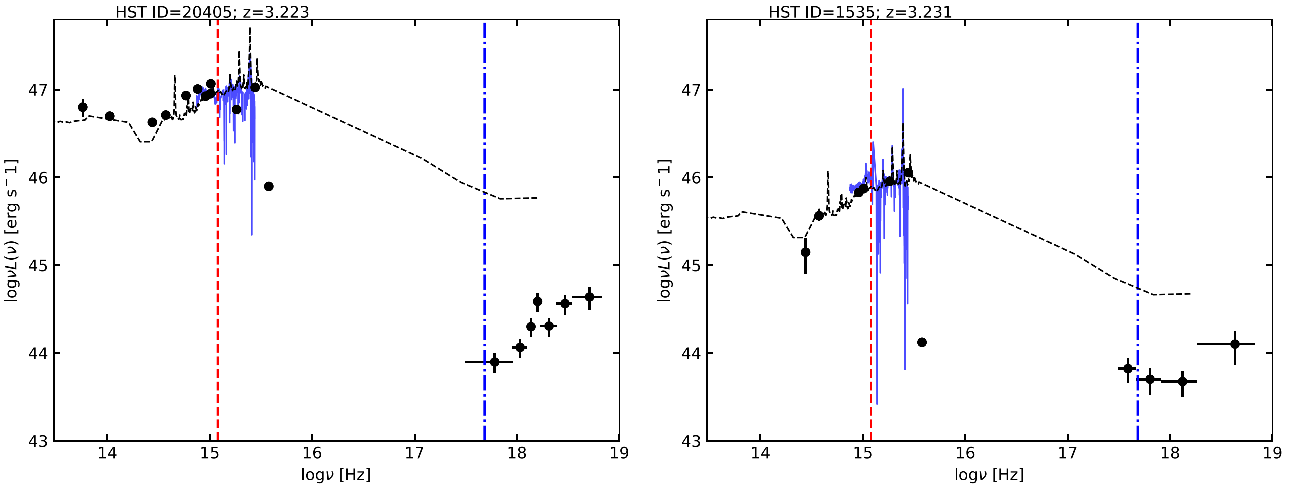

Figure C1. Rest-frame broad-band photometric spectral energy distributions for J2142−4420 (*HST* ID = 20405) and J2142−4419 (*HST* ID = 1535) from the near-infrared to the X-rays. Data are shown with black points. The MUSE plus *HST* spectrum for the two quasars is shown with a blue line. We also overplotted the SED for radio-quiet AGN published by Shang et al. (2011) as a reference. The vertical red dashed and blue dot–dashed lines mark the 2500 Å and the 2 keV energies, respectively.

This paper has been typeset from a TEX/LATEX file prepared by the author.

Published by Oxford University Press on behalf of Royal Astronomical Society